PNAS

Supporting Information for

Origami Frustration and Its Influence on Energy Landscapes of Origami Assemblies

Shixi Zang, Tuo Zhao, Diego Misseroni, and Glaucio H. Paulino

Diego Misseroni and Glaucio H. Paulino.
E-mail: diego.misseroni@unitn.it, gpaulino@princeton.edu

This PDF file includes:

Other supporting materials for this manuscript include the following:

Movies S1 to S6

Supporting Information Text

Here we present all the details of the concepts presented in the main text. The presentation is detailed to make sure that all the results are reproduceable or generalizable, e.g. generalization of frustration mechanisms with linear springs to those with nonlinear springs.

1. Details of Theoretical Formulation

The total elastic energy expression for the geometrically frustrated Kresling origami cell, $U_{\mathrm{fru}}(u,\varphi)$, includes two parts. The first part is the energy from the spring mechanism, $U_{\mathrm{spr}}(u,\varphi)$, which introduces frustration by prestressing. The second part is the energy of the standard Kresling origami cell, $U(u,\varphi)$. Therefore, we have:

$$\boxed{U_{\mathrm{fru}}(u,\varphi) = U_{\mathrm{spr}}(u,\varphi) + U(u,\varphi)} \quad [1]$$

where two independent variables, u and φ, represent the axial displacement (change in the cell height) and the twist angle (relative rotation between the top and bottom faces of the cell). These variables describe the folding and unfolding process, as shown in Fig. S1. In the following paragraphs, we present the detailed formulation of the standard Kresling cell and four different frustrated mechanism systems.

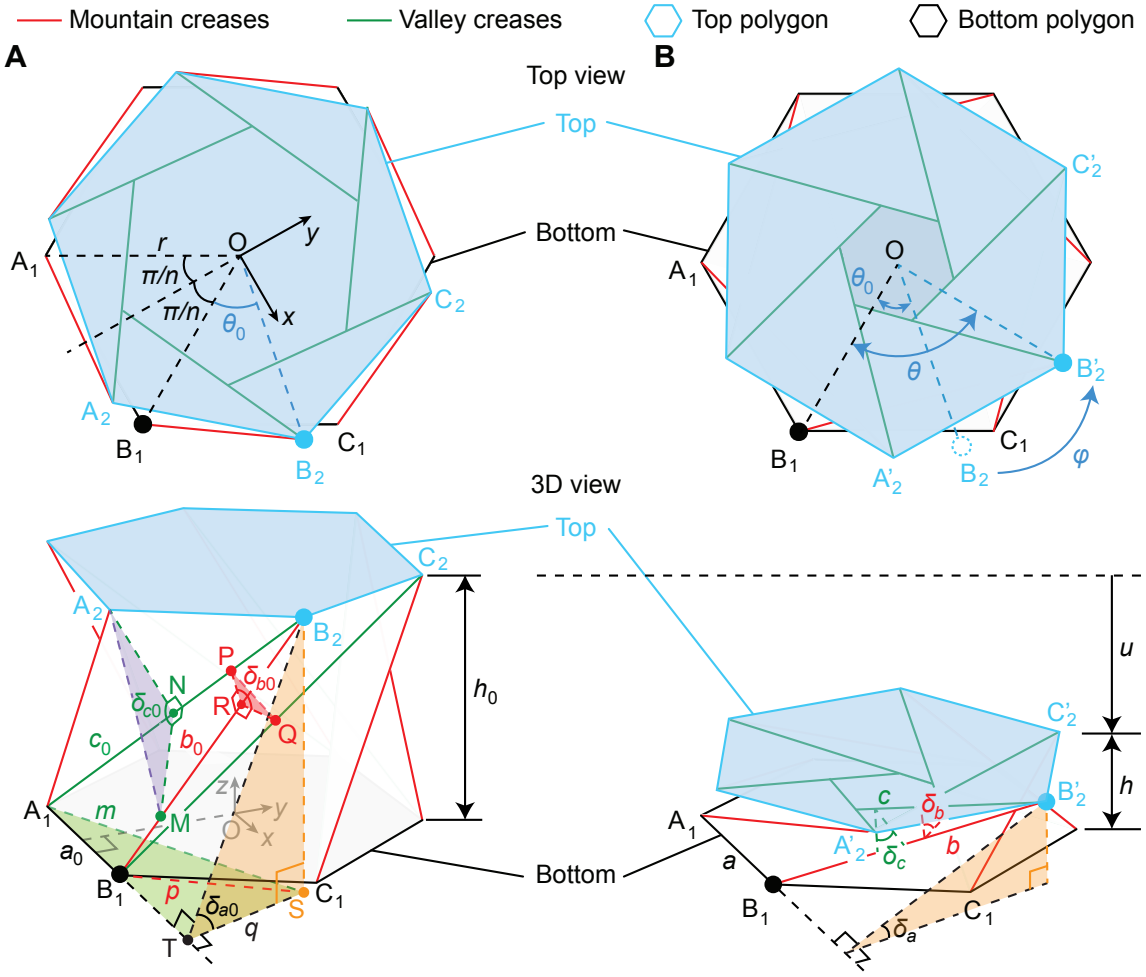

Fig. S1. Illustration of the parameters in the standard Kresling origami cell. Schematics of the (A) deployed and (B) folded configurations with geometric parameters and vertices description. The first row shows the top view, and the second row shows a perspective view. The elastic energy is described by the five-term model (b, c, δ_a, δ_b, δ_c) of Ref. (1). Figure reproduced from Ref. (1).

Standard Kresling cell. The geometry of the standard n-gon Kresling cell is defined by three intrinsic parameters: r, h_{folded}, and θ_0. Here, r is the radius of the circumscribed circle of polygon, h_{folded} is the height of the cell in the folded state, and θ_0 is the initial relative angle between the top and bottom polygons in the deployed state. Figure S1 shows the geometric parameters of Kresling cell. We define a as the length of the crease between the top/bottom polygon and the side panels. The parameters b and c are the length of mountain and valley creases connecting two adjacent side panels, respectively. The

dihedral angle between the top/bottom polygon and the side panels is denoted by δ_a. The angles δ_b and δ_c represent the dihedral angles between adjacent side panels along the mountain and valley creases, respectively. The subscript '0' refers to the initial configuration, i.e., deployed state. The expressions of these geometric parameters (see Fig. S1) are given as follows (1):

$$a_0 = a = 2r\sin(\pi/n); \tag{2}$$

$$b_0 = \sqrt{h_0^2 + 4r^2\sin^2(\theta_0/2)},\ b(u,\varphi) = \sqrt{(h_0-u)^2 + 4r^2\sin^2(\varphi/2+\theta_0/2)}; \tag{3}$$

$$c_0 = \sqrt{h_0^2 + 4r^2\sin^2(\theta_0/2+\pi/n)},\ c(u,\varphi) = \sqrt{(h_0-u)^2 + 4r^2\sin^2(\varphi/2+\theta_0/2+\pi/n)}; \tag{4}$$

$$\delta_{a0} = \arctan\frac{h_0}{2r\sin(\theta_0/2+\pi/n)\sin(\theta_0/2)},\ \delta_a(u,\varphi) = \arctan\frac{(h_0-u)}{2r\sin(\varphi/2+\theta_0/2+\pi/n)\sin(\varphi/2+\theta_0/2)}; \tag{5}$$

$$\begin{aligned}\delta_{b0} &= \pi - \arccos\frac{h_0^2\cos(\theta_0+2\pi/n) - r^2[\cos(\theta_0+\pi/n)-\cos(\pi/n)]^2}{h_0^2 + r^2[\cos(\theta_0+\pi/n)-\cos(\pi/n)]^2},\\ \delta_b(u,\varphi) &= \pi - \arccos\frac{(h_0-u)^2\cos(\varphi+\theta_0+2\pi/n) - r^2[\cos(\varphi+\theta_0+\pi/n)-\cos(\pi/n)]^2}{(h_0-u)^2 + r^2[\cos(\varphi+\theta_0+\pi/n)-\cos(\pi/n)]^2};\end{aligned} \tag{6}$$

$$\begin{aligned}\delta_{c0} &= \pi - \arccos\frac{h_0^2\cos\theta_0 - r^2[\cos(\theta_0+\pi/n)-\cos(\pi/n)]^2}{h_0^2 + r^2[\cos(\theta_0+\pi/n)-\cos(\pi/n)]^2},\\ \delta_c(u,\varphi) &= \pi - \arccos\frac{(h_0-u)^2\cos(\varphi+\theta_0) - r^2[\cos(\varphi+\theta_0+\pi/n)-\cos(\pi/n)]^2}{(h_0-u)^2 + r^2[\cos(\varphi+\theta_0+\pi/n)-\cos(\pi/n)]^2}.\end{aligned} \tag{7}$$

We assume that the creases connected to the top and bottom polygons cannot deform, so $a_0 = a$, as they are constrained by stiffer top/bottom plates (they do not deform) . Then, the elastic energy of the Kresling cell is expressed by the five-term expression as (1):

$$\begin{aligned}U(u,\varphi) = &\frac{1}{2}n_b k_{s,b}(b(u,\varphi)-b_0)^2 + \frac{1}{2}n_c k_{s,c}(c(u,\varphi)-c_0)^2\\ &+\frac{1}{2}n_a k_{r,a}(\delta_a(u,\varphi)-\delta_{a0})^2 + \frac{1}{2}n_b k_{r,b}(\delta_b(u,\varphi)-\delta_{b0})^2 + \frac{1}{2}n_c k_{r,c}(\delta_c(u,\varphi)-\delta_{c0})^2.\end{aligned} \tag{8}$$

Here, n_a, n_b, and n_c are the numbers of edge, mountain and valley creases, respectively; $k_{s,b}$ and $k_{s,b}$ are the stretching stiffnesses of the mountain and valley creases; and $k_{r,a}$, $k_{r,b}$ and $k_{r,c}$ the rotational stiffnesses of the edge, mountain, and valley creases, respectively. Table S1 lists the representative values of the parameters used in the theoretical analysis. The stiffness parameters are taken from Ref. (1).

Table S1. Geometrical and mechanical parameters of Kresling origami cell.

Parameter	Value
r (mm)	30
h_0 (mm)	46.95
θ_0 (deg)	15
n_a	12
n_b	6
n_c	6
$k_{s,b}$ (N/mm)	0.32
$k_{s,c}$ (N/mm)	3.18
$k_{r,a}$ (N·mm/rad)	0.16
$k_{r,b}$ (N·mm/rad)	0.26
$k_{r,c}$ (N·mm/rad)	0.32

Global stretch model. The global stretch model is created by adding a prestressed spring along the central axis of the standard origami cell. To describe the mechanical behavior of the frustrated Kresling cell, we use the following expression for the spring energy term:

$$U_{\rm spr}(u,\varphi) = \frac{1}{2}k_{s,e}(\Delta\ell_e - u)^2, \tag{9}$$

where $k_{s,e}$ stiffness of the spring element and $\Delta\ell_e$ the stretching length. By substituting Eqs. 8 and 9 into Eq. 1, we obtain the following expression for the total elastic energy of the global stretch model:

$$U_{\text{fru}}(u,\varphi) = \frac{1}{2}k_{s,e}(\Delta\ell_e - u)^2 + \frac{1}{2}n_b k_{s,b}(b(u,\varphi) - b_0)^2 + \frac{1}{2}n_c k_{s,c}(c(u,\varphi) - c_0)^2 + \frac{1}{2}n_a k_{r,a}(\delta_a(u,\varphi) - \delta_{a0})^2 + \frac{1}{2}n_b k_{r,b}(\delta_b(u,\varphi) - \delta_{b0})^2 + \frac{1}{2}n_c k_{r,c}(\delta_c(u,\varphi) - \delta_{c0})^2. \quad [10]$$

Since the folding of the Kresling cell can be activated by either an axial force F or a torque T, the work done by these external loads is given by:

$$W(u,\varphi) = \int F du + \int T d\varphi. \quad [11]$$

Then, the total potential energy of the frustrated cell, $\Pi(u,\varphi)$, can be expressed as:

$$\Pi(u,\varphi) = U_{\text{fru}}(u,\varphi) - W(u,\varphi). \quad [12]$$

Considering that $\Pi(u,\varphi)$ is a function of two independent variables, u and φ, the equilibrium condition is obtained from the principle of minimum total potential energy:

$$\frac{\partial\Pi}{\partial u} = 0, \quad \frac{\partial\Pi}{\partial\varphi} = 0. \quad [13]$$

Equation 13 gives the condition for free-rotation and free-translation, which are expressed as:

$$\frac{\partial U_{\text{fru}}(u,\varphi)}{\partial\varphi} = 0, \quad [14]$$

and

$$\frac{\partial U_{\text{fru}}(u,\varphi)}{\partial u} = 0. \quad [15]$$

respectively.

The energy formulation in Eq. 9, shows that, for a given stiffness $k_{s,e}$, the energy contribution from the prestressed spring can be tuned by adjusting $\Delta\ell_e$. We refer to cases with negative $\Delta\ell_e/u_{\text{m}}$ ratios as negative prestressing modes. In these cases, the spring remains contracted during the folding of the origami cell. The energy $U_{\text{fru}}(u,\varphi)$ of the frustrated Kresling cell in the negative mode is calculated using Eq. 10. In contrast, positive prestressing modes correspond to positive $\Delta\ell_e/u_{\text{m}}$ ratios. Here, the spring tends to return to its original length as the cell folds, meaning that $(\ell_e - u)$ approaches zero. Based on the relationship between $\Delta\ell_e$ and u, we define the following expression for the energy of the positive global stretch model:

$$U_{\text{fru}}(u,\varphi) = \begin{cases} U_{\text{spr}}(u,\varphi) + U(u,\varphi), & u \le \Delta\ell_e, \\ U(u,\varphi), & u > \Delta\ell_e. \end{cases} \quad [16]$$

By substituting the loading conditions of free rotation (Eq. 14) or free-translation (Eq. 15) into the energy expressions (Eqs. 10 and 16), we obtain a relationship between U_{fru} and u or φ, respectively. These relationships are illustrated in Fig. 2B.

Moreover, we observe that the curves, U_{fru} versus u, and U_{fru} versus φ, in Fig. 2B exhibit three stationary points. These points are determined by solving the two conditions in Eqs. 14 and 15. The stationary points, $(u^{\text{I}},\varphi^{\text{I}})$, $(\widetilde{u},\widetilde{\varphi})$, and $(u^{\text{II}},\varphi^{\text{II}})$, correspond to the three energy quantities. They are base energy of the first stable state, $U^{\text{I}}_{\text{fru}}$, the maximum energy between stable states, $U_{\max}$, and the base energy of the second stable state, $U^{\text{II}}_{\text{fru}}$, respectively. Thus, 6energy terms are given by:

$$U^{\text{I}}_{\text{fru}} = U_{\text{fru}}(u^{\text{I}},\varphi^{\text{I}}), \quad U_{\max} = U_{\text{fru}}(\widetilde{u},\widetilde{\varphi}), \quad U^{\text{II}}_{\text{fru}} = U_{\text{fru}}(u^{\text{II}},\varphi^{\text{II}}). \quad [17]$$

Then, we define the energy barrier, ΔU, as:

$$\boxed{\Delta U_{\text{fru}} = U_{\max} - U^{\text{I}}_{\text{fru}}.} \quad [18]$$

Table S2 (rows GS1-4) shows the energy terms of global stretch model along with the corresponding values of u and φ for different values of $\Delta\ell_e$ and a given stiffness $k_{s,e}$. Compared to the standard Kresling cell shown in row 'O', the base energy of the first stable state, $U^{\text{I}}_{\text{fru}}$, is not zero in either the negative or positive prestress modes. However, the base energy of the second stable state, $U^{\text{II}}_{\text{fru}}$, behaves differently depending on the mode. In the negative prestress mode, $U^{\text{II}}_{\text{fru}}$ always increases (see row 'GS2'). As this energy increases, the frustrated Kresling cell changes from bistable to monostable (see rows 'GS1$^+$' and 'GS2'). In the positive mode, the base energy of the second stable state either increases (row 'GS4') or stays the same (row 'GS3') depending on the value of $\Delta\ell_e$. Additionally, the energy barrier, ΔU_{fru}, always decreases as $\Delta\ell_e$ increases.

Table S2. Geometrical and mechanical parameters of frustrated models (global stretch, global rotation, and crease stretch) in Fig. 2.

Model	$k_{s,e}$ (N/mm)	$\Delta\ell_e/u_\mathrm{m}$	$k_{r,e}$ (N·mm/rad)	$\Delta\eta_e/\varphi_\mathrm{m}$	$U_\mathrm{fru}^\mathrm{I}$ (mJ)	$u^\mathrm{I}/u_\mathrm{m}$	$\varphi^\mathrm{I}/\varphi_\mathrm{m}$	$U_\mathrm{fru}^\mathrm{II}$ (mJ)	$u^\mathrm{II}/u_\mathrm{m}$	$\varphi^\mathrm{II}/\varphi_\mathrm{m}$	ΔU_fru (mJ)
O	–	–	–	–	0	0	0	11.249	0.862	0.971	31.317
GS1$^+$	0.03	-0.6	–	–	11.583	-0.016	-0.026	n/a	n/a	n/a	n/a
GS2	0.03	-0.3	–	–	2.894	-0.008	-0.014	47.462	0.641	0.813	45.668
GS3	0.03	0.5	–	–	8.018	0.016	0.026	11.249	0.862	0.971	23.850
GS4	0.03	1	–	–	32.006	0.034	0.056	11.698	0.904	0.985	13.505
GR1$^+$	–	–	18	-1	21.038	-0.028	-0.051	n/a	n/a	n/a	n/a
GR2	–	–	18	-0.5	5.252	-0.015	-0.027	55.870	0.695	0.847	52.296
GR3	–	–	18	0.6	7.531	0.020	0.036	11.249	0.862	0.971	23.787
GR4	–	–	18	1.2	30.024	0.045	0.078	12.357	0.883	0.982	12.341
CS1	0.08	-0.12	–	–	3.397	-0.017	-0.029	15.163	0.899	1.000	40.908
CS2	0.08	-0.06	–	–	0.849	-0.009	-0.014	12.365	0.883	0.987	37.424
CS3	0.08	0.3	–	–	21.240	0.049	0.075	31.171	0.768	0.892	20.071
CS4	0.08	0.6	–	–	85.010	0.107	0.159	93.148	0.651	0.785	10.255

$^+$In these models, the 2$^\mathrm{nd}$ stable state is not available.

Substituting Eqs. 10 and 12 into Eq. 13, yields the expressions for the axial force, F, and torque, T, as follows:

$$\begin{aligned} F(u,\varphi) &= \frac{\partial U_\mathrm{fru}(u,\varphi)}{\partial u} \\ &= -k_{s,e}(\Delta\ell_e - u) + n_b k_{s,b}(b(u,\varphi) - b_0)\frac{\partial b(u,\varphi)}{\partial u} + n_c k_{s,c}(c(u,\varphi) - c_0)\frac{\partial c(u,\varphi)}{\partial u} \\ &+ n_a k_{r,a}(\delta_a(u,\varphi) - \delta_{a0})\frac{\partial \delta_a(u,\varphi)}{\partial u} + n_b k_{r,b}(\delta_b(u,\varphi) - \delta_{b0})\frac{\partial \delta_b(u,\varphi)}{\partial u} + n_c k_{r,c}(\delta_c(u,\varphi) - \delta_{c0})\frac{\partial \delta_c(u,\varphi)}{\partial u}, \end{aligned} \tag{19}$$

with loading conditions expressed by Eq. 14, and

$$\begin{aligned} T(u,\varphi) &= \frac{\partial U_\mathrm{fru}(u,\varphi)}{\partial \varphi} \\ &= n_b k_{s,b}(b(u,\varphi) - b_0)\frac{\partial b(u,\varphi)}{\partial \varphi} + n_c k_{s,c}(c(u,\varphi) - c_0)\frac{\partial c(u,\varphi)}{\partial \varphi} + n_a k_{r,a}(\delta_a(u,\varphi) - \delta_{a0})\frac{\partial \delta_a(u,\varphi)}{\partial \varphi} \\ &+ n_b k_{r,b}(\delta_b(u,\varphi) - \delta_{b0})\frac{\partial \delta_b(u,\varphi)}{\partial \varphi} + n_c k_{r,c}(\delta_c(u,\varphi) - \delta_{c0})\frac{\partial \delta_c(u,\varphi)}{\partial \varphi}, \end{aligned} \tag{20}$$

with loading conditions expressed by Eq. 15.

Global rotation model. The global rotation model is obtained by adding a torsional spring whose center of rotation is located at the center of the standard origami cell. The energy associated with the prestressed spring, $U_\mathrm{spr}(u,\varphi)$, is expressed in terms of the spring stiffness $k_{r,e}$ and the rotation angle $\Delta\eta_e$ as follows:

$$\boxed{U_\mathrm{spr}(u,\varphi) = \frac{1}{2}k_{r,e}(\Delta\eta_e - \varphi)^2,} \tag{21}$$

Substituting Eqs. 8 and 21 into Eq. 1, we can write the total elastic energy, $U_\mathrm{fru}(u,\varphi)$, of the global rotation frustrated cell as follows:

$$\begin{aligned} U_\mathrm{fru}(u,\varphi) &= \frac{1}{2}k_{r,e}(\Delta\eta_e - \varphi)^2 + \frac{1}{2}n_b k_{s,b}(b(u,\varphi) - b_0)^2 + \frac{1}{2}n_c k_{s,c}(c(u,\varphi) - c_0)^2 \\ &+ \frac{1}{2}n_a k_{r,a}(\delta_a(u,\varphi) - \delta_{a0})^2 + \frac{1}{2}n_b k_{r,b}(\delta_b(u,\varphi) - \delta_{b0})^2 + \frac{1}{2}n_c k_{r,c}(\delta_c(u,\varphi) - \delta_{c0})^2. \end{aligned} \tag{22}$$

Similar to the global stretch model, the energy expression for the global rotation model shows that, for a given stiffness $k_{r,e}$, the energy terms can be tuned by varying $\Delta\eta_e$. In the negative prestressing mode, where $\Delta\eta_e/\varphi_\mathrm{m}$ is negative (with φ_m being the maximum twist angle), the spring remains deformed throughout the folding of the origami cell. As a result, the total elastic energy of the frustrated Kresling, $U_\mathrm{fru}(u,\varphi)$, is given by Eq. 22. In contrast, in the positive prestressing mode (positive $\Delta\eta_e/\varphi_\mathrm{m}$) the spring tends to return to its original rotation angle during folding. In this case, the term $(\Delta\eta_e - \varphi)$ approaches zero when the origami cell is folded. This behavior requires a modified energy expression based on the relationship between $\Delta\eta_e$ and φ, as follows:

$$U_\mathrm{fru}(u,\varphi) = \begin{cases} U_\mathrm{spr}(u,\varphi) + U(u,\varphi), & \varphi \le \Delta\eta_e, \\ U(u,\varphi), & \varphi > \Delta\eta_e. \end{cases} \tag{23}$$

The relationship between U_{fru} and u is evaluated using Eqs. 22 and 23 under the loading condition given in Eq. 14, while the relationship between U_{fru} and φ is obtained using the same equations with the loading condition in Eq. 15. The results corresponds to the curves shown in Fig. 2E.

Table S2 (rows GR1-4) shows the energy terms of global rotation model along with the corresponding values of u and φ for different values of $\Delta\eta_e$ and a given stiffness $k_{r,e}$. Compared to the standard Kresling cell shown in row 'O', the base energy of the first stable state, $U_{\text{fru}}^{\text{I}}$, is not zero in either the negative or positive prestress modes. However, the base energy of the second stable state, $U_{\text{fru}}^{\text{II}}$, behaves differently depending on the mode. In the negative prestress mode, $U_{\text{fru}}^{\text{II}}$ always increases (see row 'GR2'), excluding the monostable model 'GR1'. In the positive mode, the base energy of the second stable state either increases (row 'GR4') or stays the same (row 'GR3') depending on the value of $\Delta\eta_e$. Additionally, the energy barrier, ΔU_{fru}, always decreases as $\Delta\eta_e$ increases.

Based on the above energy formulations, the expressions for the axial force F and torque T are given as follows:

$$\begin{aligned} F(u,\varphi) &= \frac{\partial U_{\text{fru}}(u,\varphi)}{\partial u} \\ &= n_b k_{s,b}(b(u,\varphi)-b_0)\frac{\partial b(u,\varphi)}{\partial u} + n_c k_{s,c}(c(u,\varphi)-c_0)\frac{\partial c(u,\varphi)}{\partial u} + n_a k_{r,a}(\delta_a(u,\varphi)-\delta_{a0})\frac{\partial \delta_a(u,\varphi)}{\partial u} \\ &+ n_b k_{r,b}(\delta_b(u,\varphi)-\delta_{b0})\frac{\partial \delta_b(u,\varphi)}{\partial u} + n_c k_{r,c}(\delta_c(u,\varphi)-\delta_{c0})\frac{\partial \delta_c(u,\varphi)}{\partial u}, \end{aligned} \tag{24}$$

with free-rotating loading condition, Eq. 14, and

$$\begin{aligned} T(u,\varphi) &= \frac{\partial U_{\text{fru}}(u,\varphi)}{\partial \varphi} \\ &= -k_{r,e}(\Delta\eta_e-\varphi) + n_b k_{s,b}(b(u,\varphi)-b_0)\frac{\partial b(u,\varphi)}{\partial \varphi} + n_c k_{s,c}(c(u,\varphi)-c_0)\frac{\partial c(u,\varphi)}{\partial \varphi} \\ &+ n_a k_{r,a}(\delta_a(u,\varphi)-\delta_{a0})\frac{\partial \delta_a(u,\varphi)}{\partial \varphi} + n_b k_{r,b}(\delta_b(u,\varphi)-\delta_{b0})\frac{\partial \delta_b(u,\varphi)}{\partial \varphi} + n_c k_{r,c}(\delta_c(u,\varphi)-\delta_{c0})\frac{\partial \delta_c(u,\varphi)}{\partial \varphi}, \end{aligned} \tag{25}$$

with free-translating loading condition, Eq. 15.

Crease stretch model (local). This model assumes that prestressed springs introducing frustration into the Kresling cell are assumed to be aligned with the mountain ('b') and valley ('c') creases. The energy associated with the prestressed spring, $U_{\text{spr}}(u,\varphi)$, is given by:

$$\boxed{U_{\text{spr}}(u,\varphi) = \frac{1}{2}n_{e,b}k_{s,e,b}(b(u,\varphi)-b_0+\Delta\ell_{e,b})^2 + \frac{1}{2}n_{e,c}k_{s,e,c}(c(u,\varphi)-c_0+\Delta\ell_{e,c})^2,} \tag{26}$$

where $n_{e,i}$, $k_{s,e,i}$, and $\Delta\ell_{e,i}$ ($i = b$ and c) are the number, stiffness, and stretching length of the spring element along the mountain ('b') and valley ('c') creases, respectively. Based on Eq. 26, the total elastic energy $U_{\text{fru}}(u,\varphi)$ of the crease (local) stretch model is expressed as follows:

$$\begin{aligned} U_{\text{fru}}(u,\varphi) &= \frac{1}{2}n_{e,b}k_{s,e,b}(b(u,\varphi)-b_0+\Delta\ell_{e,b})^2 + \frac{1}{2}n_{e,c}k_{s,e,c}(c(u,\varphi)-c_0+\Delta\ell_{e,c})^2 + \frac{1}{2}n_b k_{s,b}(b(u,\varphi)-b_0)^2 \\ &+ \frac{1}{2}n_c k_{s,c}(c(u,\varphi)-c_0)^2 + \frac{1}{2}n_a k_{r,a}(\delta_a(u,\varphi)-\delta_{a0})^2 + \frac{1}{2}n_b k_{r,b}(\delta_b(u,\varphi)-\delta_{b0})^2 + \frac{1}{2}n_c k_{r,c}(\delta_c(u,\varphi)-\delta_{c0})^2. \end{aligned} \tag{27}$$

Based on the above energy formulations, the expressions for the axial force F and torque T are given as follows:

$$\begin{aligned} F(u,\varphi) &= \frac{\partial U_{\text{fru}}(u,\varphi)}{\partial u} \\ &= n_{e,b}k_{s,e,b}(b(u,\varphi)-b_0+\Delta\ell_{e,b})\frac{\partial b(u,\varphi)}{\partial u} + n_{e,c}k_{s,e,c}(c(u,\varphi)-c_0+\Delta\ell_{e,c})\frac{\partial c(u,\varphi)}{\partial u} \\ &+ n_b k_{s,b}(b(u,\varphi)-b_0)\frac{\partial b(u,\varphi)}{\partial u} + n_c k_{s,c}(c(u,\varphi)-c_0)\frac{\partial c(u,\varphi)}{\partial u} + n_a k_{r,a}(\delta_a(u,\varphi)-\delta_{a0})\frac{\partial \delta_a(u,\varphi)}{\partial u} \\ &+ n_b k_{r,b}(\delta_b(u,\varphi)-\delta_{b0})\frac{\partial \delta_b(u,\varphi)}{\partial u} + n_c k_{r,c}(\delta_c(u,\varphi)-\delta_{c0})\frac{\partial \delta_c(u,\varphi)}{\partial u}, \end{aligned} \tag{28}$$

with free-rotating loading condition, Eq. 14, and

$$
\begin{aligned}
T(u,\varphi) &= \frac{\partial U_{\text{fru}}(u,\varphi)}{\partial \varphi} \\
&= n_{e,b}k_{s,e,b}(b(u,\varphi)-b_0+\Delta\ell_{e,b})\frac{\partial b(u,\varphi)}{\partial \varphi} + n_{e,c}k_{s,e,c}(c(u,\varphi)-c_0+\Delta\ell_{e,c})\frac{\partial c(u,\varphi)}{\partial \varphi} \\
&+ n_b k_{s,b}(b(u,\varphi)-b_0)\frac{\partial b(u,\varphi)}{\partial \varphi} + n_c k_{s,c}(c(u,\varphi)-c_0)\frac{\partial c(u,\varphi)}{\partial \varphi} + n_a k_{r,a}(\delta_a(u,\varphi)-\delta_{a0})\frac{\partial \delta_a(u,\varphi)}{\partial \varphi} \\
&+ n_b k_{r,b}(\delta_b(u,\varphi)-\delta_{b0})\frac{\partial \delta_b(u,\varphi)}{\partial \varphi} + n_c k_{r,c}(\delta_c(u,\varphi)-\delta_{c0})\frac{\partial \delta_c(u,\varphi)}{\partial \varphi}.
\end{aligned}
\tag{29}
$$

with free-translating loading condition, Eq. 15.

For the sake of manufacturing simplicity, we simplify Eqs. 26-29 by setting $n_{e,c}=0$, $n_{e,b}=n_e$, $k_{s,e,b}=k_{s,e}$, and $\Delta\ell_{e,b}=\Delta\ell_e$. These assumptions correspond to the crease stretch model where the springs are aligned only along the mountain creases, as shown in the schematic and plots in Fig. 2G and H. The simplified expressions are given as follows:

$$
\boxed{U_{\text{spr}}(u,\varphi) = \frac{1}{2}n_e k_{s,e}(b(u,\varphi)-b_0+\Delta\ell_e)^2,}
\tag{30}
$$

$$
\begin{aligned}
U_{\text{fru}}(u,\varphi) &= \frac{1}{2}n_e k_{s,e}(b(u,\varphi)-b_0+\Delta\ell_e)^2 + \frac{1}{2}n_b k_{s,b}(b(u,\varphi)-b_0)^2 + \frac{1}{2}n_c k_{s,c}(c(u,\varphi)-c_0)^2 \\
&+ \frac{1}{2}n_a k_{r,a}(\delta_a(u,\varphi)-\delta_{a0})^2 + \frac{1}{2}n_b k_{r,b}(\delta_b(u,\varphi)-\delta_{b0})^2 + \frac{1}{2}n_c k_{r,c}(\delta_c(u,\varphi)-\delta_{c0})^2,
\end{aligned}
\tag{31}
$$

$$
\begin{aligned}
F(u,\varphi) &= \frac{\partial U_{\text{fru}}(u,\varphi)}{\partial u} \\
&= n_e k_{s,e}(b(u,\varphi)-b_0+\Delta\ell_{e,b})\frac{\partial b(u,\varphi)}{\partial u} + n_b k_{s,b}(b(u,\varphi)-b_0)\frac{\partial b(u,\varphi)}{\partial u} + n_c k_{s,c}(c(u,\varphi)-c_0)\frac{\partial c(u,\varphi)}{\partial u} \\
&+ n_a k_{r,a}(\delta_a(u,\varphi)-\delta_{a0})\frac{\partial \delta_a(u,\varphi)}{\partial u} + n_b k_{r,b}(\delta_b(u,\varphi)-\delta_{b0})\frac{\partial \delta_b(u,\varphi)}{\partial u} + n_c k_{r,c}(\delta_c(u,\varphi)-\delta_{c0})\frac{\partial \delta_c(u,\varphi)}{\partial u},
\end{aligned}
\tag{32}
$$

and

$$
\begin{aligned}
T(u,\varphi) &= \frac{\partial U_{\text{fru}}(u,\varphi)}{\partial \varphi} \\
&= n_e k_{s,e}(b(u,\varphi)-b_0+\Delta\ell_{e,b})\frac{\partial b(u,\varphi)}{\partial \varphi} + n_b k_{s,b}(b(u,\varphi)-b_0)\frac{\partial b(u,\varphi)}{\partial \varphi} + n_c k_{s,c}(c(u,\varphi)-c_0)\frac{\partial c(u,\varphi)}{\partial \varphi} \\
&+ n_a k_{r,a}(\delta_a(u,\varphi)-\delta_{a0})\frac{\partial \delta_a(u,\varphi)}{\partial \varphi} + n_b k_{r,b}(\delta_b(u,\varphi)-\delta_{b0})\frac{\partial \delta_b(u,\varphi)}{\partial \varphi} + n_c k_{r,c}(\delta_c(u,\varphi)-\delta_{c0})\frac{\partial \delta_c(u,\varphi)}{\partial \varphi}.
\end{aligned}
\tag{33}
$$

Equations 30 and 31 show that the energy terms can be tuned by varying $\Delta\ell_e$ for a given stiffness $k_{s,e}$. In the negative prestressing mode, the spring in the crease stretch model remains deformed as the origami cell folds, so the total elastic energy $U_{\text{fru}}(u,\varphi)$, is given by Eq. 31. In contrast, in the positive prestressing mode, the spring returns to its original length during folding, causing the term $(b(u,\varphi)-b_0+\Delta\ell_{e,b})$ to approach zero. This behavior leads to a modified energy expression based on the relationship between $\Delta\ell_e$ and $|(b(u,\varphi)-b_0)|$, as follows:

$$
U_{\text{fru}}(u,\varphi) = \begin{cases} U_{\text{spr}}(u,\varphi)+U(u,\varphi), & |b(u,\varphi)-b_0| \le \Delta\ell_e, \\ U(u,\varphi), & |b(u,\varphi)-b_0| > \Delta\ell_e. \end{cases}
\tag{34}
$$

We illustrate the relationship between U_{fru} and both u and φ, as obtained from Eqs. 31 and 34 in Fig. 2H. This analysis assumes $n_e = n_b/2$, and uses the loading conditions given in Eqs. 14 and 15.

Table S2 (rows CS1-4) presents the energy terms of the crease (local) stretch model, along with the corresponding values of u and φ, calculated for various $\Delta\ell_e$ and a fixed stiffness $k_{s,e}$. Unlike the global prestressed models, the base energy of the two stable states, $U^{\text{I}}_{\text{fru}}$ and $U^{\text{II}}_{\text{fru}}$ increases in both negative (rows 'CS1' and 'CS2') and positive (rows 'CS3' and 'CS4') prestressing modes. On the other hand, the energy barrier, ΔU_{fru}, always decreases as $\Delta\ell_e$ increases.

Crease rotation model (local). The crease (local) rotation model assumes that prestressed torsional springs, which introduce frustration into the Kresling cell, are inserted along the creases. The elastic energy $U_{\mathrm{spr}}(u,\varphi)$ associated with these springs is given by:

$$\boxed{U_{\mathrm{spr}}(u,\varphi)=\sum_{i=a,\ b,\ c}\frac{1}{2}n_{e,i}k_{r,e,i}(\delta_i(u,\varphi)-\delta_{i0}+\Delta\eta_{e,i})^2,} \tag{35}$$

where $n_{e,i}$, $k_{r,e,i}$, and $\Delta\eta_{e,i}$ ($i=a,\ b,$ and c) are the number, stiffness, and rotating angles of the spring element placed along the top/bottom ('a'), mountain ('b') and valley ('c') creases, respectively. Based on Eq. 35, the total elastic energy $U_{\mathrm{fru}}(u,\varphi)$ for the crease rotation model can be written as:

$$\begin{aligned}U_{\mathrm{fru}}(u,\varphi)=&\sum_{i=a,\ b,\ c}\frac{1}{2}n_{e,i}k_{r,e,i}(\delta_i(u,\varphi)-\delta_{i0}+\Delta\eta_{e,i})^2+\frac{1}{2}n_bk_{s,b}(b(u,\varphi)-b_0)^2+\frac{1}{2}n_ck_{s,c}(c(u,\varphi)-c_0)^2\\&+\frac{1}{2}n_ak_{r,a}(\delta_a(u,\varphi)-\delta_{a0})^2+\frac{1}{2}n_bk_{r,b}(\delta_b(u,\varphi)-\delta_{b0})^2+\frac{1}{2}n_ck_{r,c}(\delta_c(u,\varphi)-\delta_{c0})^2.\end{aligned} \tag{36}$$

As with the previously analyzed frustrating models, the expressions for axial force F and torque T are derived based on the principle of minimum total potential energy, as follows:

$$\begin{aligned}F(u,\varphi)&=\frac{\partial U_{\mathrm{fru}}(u,\varphi)}{\partial u}\\&=\sum_{i=a,\ b,\ c}n_{e,i}k_{r,e,i}(\delta_i(u,\varphi)-\delta_{i0}+\Delta\eta_{e,i})\frac{\partial\delta_i(u,\varphi)}{\partial u}+n_bk_{s,b}(b(u,\varphi)-b_0)\frac{\partial b(u,\varphi)}{\partial u}\\&+n_ck_{s,c}(c(u,\varphi)-c_0)\frac{\partial c(u,\varphi)}{\partial u}+n_ak_{r,a}(\delta_a(u,\varphi)-\delta_{a0})\frac{\partial\delta_a(u,\varphi)}{\partial u}+n_bk_{r,b}(\delta_b(u,\varphi)-\delta_{b0})\frac{\partial\delta_b(u,\varphi)}{\partial u}\\&+n_ck_{r,c}(\delta_c(u,\varphi)-\delta_{c0})\frac{\partial\delta_c(u,\varphi)}{\partial u},\end{aligned} \tag{37}$$

and

$$\begin{aligned}T(u,\varphi)&=\frac{\partial U_{\mathrm{fru}}(u,\varphi)}{\partial\varphi}\\&=\sum_{i=a,\ b,\ c}n_{e,i}k_{r,e,i}(\delta_i(u,\varphi)-\delta_{i0}+\Delta\eta_{e,i})\frac{\partial\delta_i(u,\varphi)}{\partial\varphi}+n_bk_{s,b}(b(u,\varphi)-b_0)\frac{\partial b(u,\varphi)}{\partial\varphi}\\&+n_ck_{s,c}(c(u,\varphi)-c_0)\frac{\partial c(u,\varphi)}{\partial\varphi}+n_ak_{r,a}(\delta_a(u,\varphi)-\delta_{a0})\frac{\partial\delta_a(u,\varphi)}{\partial\varphi}+n_bk_{r,b}(\delta_b(u,\varphi)-\delta_{b0})\frac{\partial\delta_b(u,\varphi)}{\partial\varphi}\\&+n_ck_{r,c}(\delta_c(u,\varphi)-\delta_{c0})\frac{\partial\delta_c(u,\varphi)}{\partial\varphi}.\end{aligned} \tag{38}$$

Here, we perform a theoretical analysis of the crease (local) rotation model using the example shown in Fig. S2A, where the torsional springs are placed only along the top and bottom creases ('a'). Under this assumption, $n_e=n_a$, allowing Eqs. 35-38 to be simplified as:

$$\boxed{U_{\mathrm{spr}}(u,\varphi)=\frac{1}{2}n_ek_{r,e}(\delta_a(u,\varphi)-\delta_{a0}+\Delta\eta_e)^2,} \tag{39}$$

$$\begin{aligned}U_{\mathrm{fru}}(u,\varphi)=&\frac{1}{2}n_ek_{r,e}(\delta_a(u,\varphi)-\delta_{a0}+\Delta\eta_e)^2+\frac{1}{2}n_bk_{s,b}(b(u,\varphi)-b_0)^2+\frac{1}{2}n_ck_{s,c}(c(u,\varphi)-c_0)^2\\&+\frac{1}{2}n_ak_{r,a}(\delta_a(u,\varphi)-\delta_{a0})^2+\frac{1}{2}n_bk_{r,b}(\delta_b(u,\varphi)-\delta_{b0})^2+\frac{1}{2}n_ck_{r,c}(\delta_c(u,\varphi)-\delta_{c0})^2,\end{aligned} \tag{40}$$

$$\begin{aligned}F(u,\varphi)&=\frac{\partial U_{\mathrm{fru}}(u,\varphi)}{\partial u}\\&=n_ek_{r,e}(\delta_a(u,\varphi)-\delta_{a0}+\Delta\eta_e)\frac{\partial\delta_a(u,\varphi)}{\partial u}+n_bk_{s,b}(b(u,\varphi)-b_0)\frac{\partial b(u,\varphi)}{\partial u}+n_ck_{s,c}(c(u,\varphi)-c_0)\frac{\partial c(u,\varphi)}{\partial u}\\&+n_ak_{r,a}(\delta_a(u,\varphi)-\delta_{a0})\frac{\partial\delta_a(u,\varphi)}{\partial u}+n_bk_{r,b}(\delta_b(u,\varphi)-\delta_{b0})\frac{\partial\delta_b(u,\varphi)}{\partial u}+n_ck_{r,c}(\delta_c(u,\varphi)-\delta_{c0})\frac{\partial\delta_c(u,\varphi)}{\partial u},\end{aligned} \tag{41}$$

and

$$T(u,\varphi) = \frac{\partial U_{\text{fru}}(u,\varphi)}{\partial \varphi}$$
$$= n_e k_{r,e}(\delta_a(u,\varphi) - \delta_{a0} + \Delta\eta_e)\frac{\partial \delta_a(u,\varphi)}{\partial \varphi} + n_b k_{s,b}(b(u,\varphi) - b_0)\frac{\partial b(u,\varphi)}{\partial \varphi} + n_c k_{s,c}(c(u,\varphi) - c_0)\frac{\partial c(u,\varphi)}{\partial \varphi} \quad [42]$$
$$+ n_a k_{r,a}(\delta_a(u,\varphi) - \delta_{a0})\frac{\partial \delta_a(u,\varphi)}{\partial \varphi} + n_b k_{r,b}(\delta_b(u,\varphi) - \delta_{b0})\frac{\partial \delta_b(u,\varphi)}{\partial \varphi} + n_c k_{r,c}(\delta_c(u,\varphi) - \delta_{c0})\frac{\partial \delta_c(u,\varphi)}{\partial \varphi}.$$

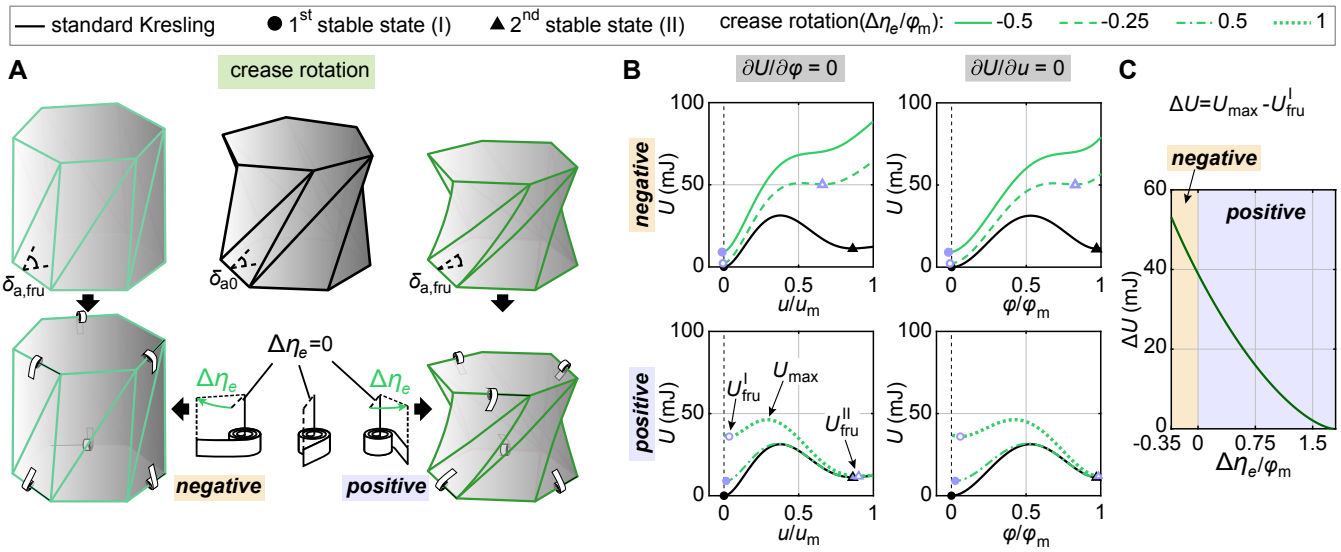

Fig. S2. Theoretical model of crease (local) rotation frustrated cell. (A) Standard Kresling origami (top-middle) and two frustrated models (top-left and top-right). The left model has six deformed torsional springs that increase the dihedral angles (negative prestress). The right model has six deformed torsional springs that decrease the dihedral angles (positive prestress). Here, $\Delta\eta_e$ denotes the rotating angle of the torsional spring. The symbols δ_{a0} and $\delta_{a,\text{fru}}$ denote the dihedral angles between the top/bottom polygon and side panels in the standard and the frustrated models, respectively. (B) Reprogrammable energy landscapes. Top: intrinsic energy landscape (black curve) versus tunable landscapes (green curves) with the negative prestress model. Bottom: intrinsic energy landscape (black curve) versus tunable landscapes (green curves) with the positive prestress model. Left: the elastic energy U versus the normalized axial displacement u/u_m under axial loading with free-rotation. Right: the elastic energy U versus the normalized twist angle φ/φ_m under torsional loading with free-translation. (C) Continuously tunable energy barrier with the global stretch feature. Normalized length changes of the spring $\Delta\eta_e/\varphi_m$ versus the energy barrier ΔU, which is defined as the maximum energy of a frustrated model U_{max} minus the energy at the first stable state $U^{\text{I}}_{\text{fru}}$.

Equations 39 and 40 demonstrate that the energy landscape of the crease rotation model can be tuned by varying $\Delta\eta_e$ for a given stiffness $k_{r,e}$. In this model, a negative $\Delta\eta_e$ defines the negative prestressing mode, which corresponds to deploying the Kresling origami cell and increasing its dihedral angles. In this mode, the torsional spring remains deformed during folding, so the total elastic energy $U_{\text{fru}}(u,\varphi)$ is given by Eq. 40. In contrast, the positive prestressing mode is defined by a positive $\Delta\eta_e$, which corresponds to folding the origami cell and decreasing the dihedral angles. In this case, as the cell folds, the spring returns to its original rotation angle, causing the term $(\delta_a(u,\varphi) - \delta_{a0} + \Delta\eta_e)$ to approach zero. As a result, the energy expression is modified based on the relationship between $\Delta\eta_e$ and $|\delta_a(u,\varphi) - \delta_{a0}|$, as follows:

$$U_{\text{fru}}(u,\varphi) = \begin{cases} U_{\text{spr}}(u,\varphi) + U(u,\varphi), & |\delta_a(u,\varphi) - \delta_{a0}| \le \Delta\eta_e, \\ U(u,\varphi), & |\delta_a(u,\varphi) - \delta_{a0}| > \Delta\eta_e. \end{cases} \quad [43]$$

The relationship between U_{fru} and both u and φ, as obtained from Eqs. 40 and 43, are shown in Fig. S2B.

Table S3 shows the energy terms of the crease (local) rotation model, with the corresponding u and φ calculated for various $\Delta\eta_e$ values and a given stiffness $k_{r,e}$. For the first stable state, the base energy U^I_{fru} is non-zero in both negative and positive prestressing modes, unlike the standard Kresling cell shown in row 'O'. However, the base energy of the second stable state, U^{II}_{fru}, behaves differently depending on the prestressing mode. In the negative prestressing mode, this energy is not reported for model 'CR1' because the increasing energy causes the Kresling origami cell to switch from bistable to monostable. A comparison between models 'O' and 'CR2' further shows that U^{II}_{fru} always increases in the negative mode. In the positive prestressing mode, the base energy at the second stable state can either increase (row 'CR4') or remain unchanged (row 'CR3'), depending on the value of $\Delta\eta_e$. Additionally, the last column of Table S3 shows that the energy barrier ΔU_{fru} consistently decreases as $\Delta\eta_e$ increases.

2. Nonlinear Spring Model

The formulations described above are based on a linear spring model, where $k_{s,e}$ or $k_{r,e}$ are constant. In this section, we extend the theoretical analysis of the four frustrated mechanism systems presented earlier by introducing nonlinear springs, and we

Table S3. Geometrical and mechanical parameters of frustrated model (crease rotation) in Fig. S2

Model	$k_{r,e}$ (N·mm/rad)	$\Delta\eta_e/\varphi_{\mathrm{m}}$	$U_{\mathrm{fru}}^{\mathrm{I}}$ (mJ)	$u^{\mathrm{I}}/u_{\mathrm{m}}$	$\varphi^{\mathrm{I}}/\varphi_{\mathrm{m}}$	$U_{\mathrm{fru}}^{\mathrm{II}}$ (mJ)	$u^{\mathrm{II}}/u_{\mathrm{m}}$	$\varphi^{\mathrm{II}}/\varphi_{\mathrm{m}}$	ΔU_{fru} (mJ)
O	–	–	0	0	0	11.249	0.862	0.971	31.317
CR1^{+}	5	-0.5	9.061	-0.012	-0.021	n/a	n/a	n/a	n/a
CR2	5	-0.25	2.263	-0.006	-0.011	50.315	0.660	0.827	48.762
CR3	5	0.5	9.026	0.015	0.026	11.249	0.862	0.971	22.292
CR4	5	1	35.995	0.035	0.060	11.977	0.902	0.985	10.270

$^{+}$In this model, the 2$^{\mathrm{nd}}$ stable state is not available.

present the general expressions for the nonlinear frustrated Kresling origami structure.

Global stretch model (nonlinear). In this frustration model, the spring force–displacement relationship is defined as $P_{\mathrm{gs}} = P_{\mathrm{gs}}(\ell_e)$, where P_{gs} is the axial force and ℓ_e is the current length of the spring. The spring length is given by $\ell_e = \ell_{e,0} + x$, where $\ell_{e,0}$ is the rest length and x the spring deformation. When the nonlinear spring is incorporated into the global stretch model, the deformation is defined as $x = \Delta\ell_e - u$, with u being the axial displacement of the Kresling cell. As a result, the relationship between the spring axial force P_{gs} and the displacement u is expressed as:

$$P_{\mathrm{gs}} = P_{\mathrm{gs}}(\ell_{e,0} + \Delta\ell_e - u). \tag{44}$$

Based on Eq. 44, the elastic energy of the spring, $U_{\mathrm{spr}}(u,\varphi)$, is given by (cf. Eq. 9 for the linear case):

$$\boxed{U_{\mathrm{spr}}(u,\varphi) = \mathrm{sgn}(\Delta\ell_e - u)\int_0^{\Delta\ell_e - u} P_{\mathrm{gs}}(\ell_{e,0} + x)dx.} \tag{45}$$

By substituting Eqs. 45 and 8 into Eq. 1, the total elastic energy of the nonlinear global stretch model, $U_{\mathrm{fru}}(u,\varphi)$, is obtained as:

$$\begin{aligned} U_{\mathrm{fru}}(u,\varphi) &= \mathrm{sgn}(\Delta\ell_e - u)\int_0^{\Delta\ell_e - u} P_{\mathrm{gs}}(\ell_{e,0} + x)dx + \frac{1}{2}n_b k_{s,b}(b(u,\varphi) - b_0)^2 + \frac{1}{2}n_c k_{s,c}(c(u,\varphi) - c_0)^2 \\ &+ \frac{1}{2}n_a k_{r,a}(\delta_a(u,\varphi) - \delta_{a0})^2 + \frac{1}{2}n_b k_{r,b}(\delta_b(u,\varphi) - \delta_{b0})^2 + \frac{1}{2}n_c k_{r,c}(\delta_c(u,\varphi) - \delta_{c0})^2 \end{aligned} \tag{46}$$

which can be compared with the equivalent expression for frustration induced by a linear spring, Eq. 10.

We derive the axial force and torque by substituting Eq. 46 into the expressions $\partial U_{\mathrm{fru}}(u,\varphi)/\partial u$ and $\partial U_{\mathrm{fru}}(u,\varphi)/\partial\varphi$. The resulting expression for the axial force $F(u,\varphi)$ is given as:

$$\begin{aligned} F(u,\varphi) &= \frac{\partial U_{\mathrm{fru}}(u,\varphi)}{\partial u} \\ &= -\mathrm{sgn}(\Delta\ell_e - u)P_{\mathrm{gs}}(\ell_{e,0} + \Delta\ell_e - u) + n_b k_{s,b}(b(u,\varphi) - b_0)\frac{\partial b(u,\varphi)}{\partial u} + n_c k_{s,c}(c(u,\varphi) - c_0)\frac{\partial c(u,\varphi)}{\partial u} \\ &+ n_a k_{r,a}(\delta_a(u,\varphi) - \delta_{a0})\frac{\partial \delta_a(u,\varphi)}{\partial u} + n_b k_{r,b}(\delta_b(u,\varphi) - \delta_{b0})\frac{\partial \delta_b(u,\varphi)}{\partial u} + n_c k_{r,c}(\delta_c(u,\varphi) - \delta_{c0})\frac{\partial \delta_c(u,\varphi)}{\partial u}, \end{aligned} \tag{47}$$

while the torque, $T(u,\varphi)$, is evaluated by Eq. 20.

Here, we present an example of a nonlinear frustrated model that includes a conical spring placed inside the origami structure and aligned with its central axis (Fig. S3A). The nonlinear force–displacement behavior $P_{\mathrm{gs}}(\ell_e)$ of the conical spring (2) is given by:

$$P_{\mathrm{gs}}(\ell_e) = \begin{cases} K_{\mathrm{R}}(\ell_{e,0} - \ell_e), & \ell_e \in [\ell_{e,\mathrm{T}}, \ell_{e,0}], \\ (K_1/2)^{3/2}\left\{1 - \left[1 - 2\left[1 - \left(1 + K_2/(K_1^2)\right)^{1/2}\right]\right]^{1/2}\right\}^3, & \ell_e \in [\ell_{e,\mathrm{S}}, \ell_{e,\mathrm{T}}], \end{cases} \tag{48}$$

where

$$K_{\mathrm{R}}=\frac{Gd^4}{2N_{\mathrm{A}}(D_1^2+D_2^2)(D_1+D_2)},\quad K_1=K_3-\frac{K_2}{3K_3},\quad K_2=-\frac{K_6}{K_5},$$

$$K_3=\left\{\frac{K_4}{16}+\left[\left(\frac{K_4}{16}\right)^2+\left(\frac{K_2}{3}\right)^3\right]^{1/2}\right\}^{1/3},\quad K_4=\left(\frac{K_7-\ell_{e,0}+\ell_e}{K_5}\right)^2,\quad K_5=-\frac{2D_1^4N_{\mathrm{A}}}{Gd^4(D_2-D_1)},\tag{49}$$

$$K_6=-\frac{3}{8(D_2-D_1)}\left(\frac{Gd^4(\ell_{\mathrm{A}}-\ell_{\mathrm{S}})^4}{N_{\mathrm{A}}}\right)^{1/3},\quad K_7=(\ell_{\mathrm{A}}-\ell_{\mathrm{S}})\frac{D_2}{D_2-D_1},\quad \ell_{e,\mathrm{A}}=\ell_{e,0}-N_id,$$

$$\ell_{e,\mathrm{S}}=\left\{\max\left[0,\ (N_{\mathrm{A}}d)^2-\frac{1}{4}(D_2-D_1)^2\right]\right\}^{1/2},\quad \ell_{e,\mathrm{T}}=\ell_{e,0}-\frac{(\ell_{e,\mathrm{A}}-\ell_{e,\mathrm{S}})(D_1^2+D_2^2)(D_1+D_2)}{4D_2^3}.$$

Based on the design parameters (D_1, D_2, d, $\ell_{e,0}$, N_i, N_A, and G) listed in Table S4, we compare the linear and nonlinear global stretch models in Fig. S3B. The results show that the energy landscape is influenced by the nonlinear prestressed spring (orange dashed line), with the base energy of both stable states increasing. The main difference between the linear (blue line) and nonlinear models emerges near the second stable state, due to the variation in axial force P_{gs} at large stretching lengths $\Delta\ell_e$.

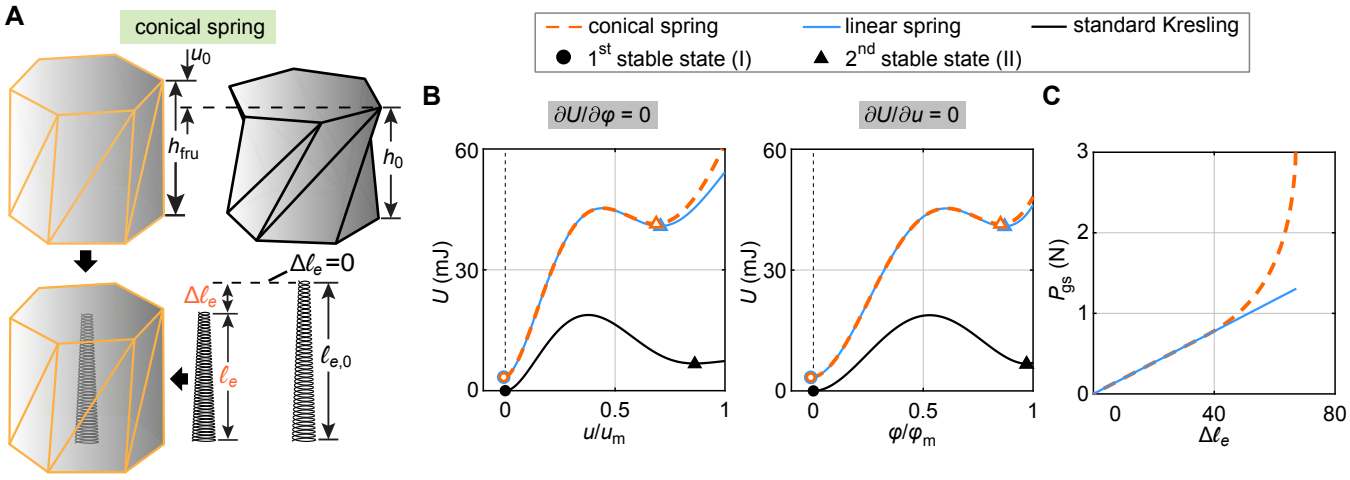

Fig. S3. Frustrated model with nonlinear spring. (A) Global stretch model with a conical spring. Here, h_0 denotes the height of the standard Kresling cell, h_{fru} is the height of the frustrated cell, and u_0 is the height difference. (B) Reprogrammable energy landscapes achieved by conical and linear springs. Left: the elastic energy U versus the normalized axial displacement u/u_m under axial loading with free-rotation. Right: the elastic energy U versus the normalized twist angle φ/φ_m under torsional loading with free-translation. (C) Mechanical response of conical and linear springs P_{gs} versus deformed length $\Delta\ell_e$.

Table S4. Geometrical and mechanical parameters of the conical spring.

Parameter	Value
D_1 (mm)	9
D_2 (mm)	15
d (mm)	1
$\ell_{e,0}$ (mm)	75
N_i	1.5
N_{A}	7
G (MPa)	2000

Global rotation model (nonlinear). In this frustration model, the spring torque–rotation relationship is defined as $T_{\mathrm{gr}}=T_{\mathrm{gr}}(\eta_e)$, where T_{gr} is the torque and η_e is the current rotation of the spring. The spring rotation is given by $\eta_e=\eta_{e,0}+x$, where $\eta_{e,0}$ is the rest angle and x the spring deformation. When the nonlinear spring is incorporated into the global rotation model, the deformation is defined as $x=\Delta\eta_e-\varphi$, with φ being the rotation of the Kresling cell. As a result, the relationship between the torque T_{gr} and the rotation φ is expressed as:

$$T_{\mathrm{gr}}=T_{\mathrm{gr}}(\eta_{e,0}+\Delta\eta_e-\varphi).\tag{50}$$

Based on Eq. 50, the elastic energy of the nonlinear torsional spring is expressed as (cf. Eq. 21 for the linear case):

$$\boxed{U_{\text{spr}}(u,\varphi) = \text{sgn}(\Delta\eta_e - \varphi)\int_0^{\Delta\eta_e-\varphi} T_{\text{gr}}(\eta_{e,0}+x)dx.} \tag{51}$$

By combining the energy expression of the nonlinear spring, Eq. 51, with that of the standard Kresling cell, Eq. 8, we obtain the total elastic energy of the nonlinear global rotation model as follows:

$$\begin{aligned} U_{\text{fru}}(u,\varphi) &= \text{sgn}(\Delta\eta_e - \varphi)\int_0^{\Delta\eta_e-\varphi} T_{\text{gr}}(\eta_{e,0}+x)dx + \frac{1}{2}n_b k_{s,b}(b(u,\varphi)-b_0)^2 + \frac{1}{2}n_c k_{s,c}(c(u,\varphi)-c_0)^2 \\ &+ \frac{1}{2}n_a k_{r,a}(\delta_a(u,\varphi)-\delta_{a0})^2 + \frac{1}{2}n_b k_{r,b}(\delta_b(u,\varphi)-\delta_{b0})^2 + \frac{1}{2}n_c k_{r,c}(\delta_c(u,\varphi)-\delta_{c0})^2, \end{aligned} \tag{52}$$

We derive the axial force and torque by substituting Eq. 52 into the expressions $\partial U_{\text{fru}}(u,\varphi)/\partial u$ and $\partial U_{\text{fru}}(u,\varphi)/\partial\varphi$. The resulting expression for the axial force is given as:

$$\begin{aligned} T(u,\varphi) &= \frac{\partial U_{\text{fru}}(u,\varphi)}{\partial\varphi} \\ &= -\text{sgn}(\Delta\eta_e-\varphi)T_{\text{gr}}(\eta_{e,0}+\Delta\eta_e-\varphi) + n_b k_{s,b}(b(u,\varphi)-b_0)\frac{\partial b(u,\varphi)}{\partial\varphi} + n_c k_{s,c}(c(u,\varphi)-c_0)\frac{\partial c(u,\varphi)}{\partial\varphi} \\ &+ n_a k_{r,a}(\delta_a(u,\varphi)-\delta_{a0})\frac{\partial\delta_a(u,\varphi)}{\partial\varphi} + n_b k_{r,b}(\delta_b(u,\varphi)-\delta_{b0})\frac{\partial\delta_b(u,\varphi)}{\partial\varphi} + n_c k_{r,c}(\delta_c(u,\varphi)-\delta_{c0})\frac{\partial\delta_c(u,\varphi)}{\partial\varphi}, \end{aligned} \tag{53}$$

which can be compared with the equivalent expression for frustration induced by a linear spring, Eq. 25. Notice that, in this case, the axial force is evaluated by the original Eq. 24

Crease stretch model (nonlinear, local). In this frustration model, the spring force–displacement relationship is defined as $P_{\text{cs}} = P_{\text{cs}}(\ell_e)$, where P_{cs} is the axial force and ℓ_e is the current length of the spring. The spring length is given by $\ell_e = \ell_{e,0} + x$, where $\ell_{e,0}$ is the rest length and x is the spring deformation. When the nonlinear spring is placed along the mountain creases of the Kresling cell, the deformation is given by $x = (b(u,\varphi) - b_0 + \Delta\ell_{e,b})$, where $b(u,\varphi)$ is the current mountain crease length, b_0 is its initial value, and $\Delta\ell_{e,b}$ is the prestretch. Similarly, when the spring is placed along the valley creases, the deformation is $x = (c(u,\varphi) - c_0 + \Delta\ell_{e,c})$, where $c(u,\varphi)$ is the current mountain crease length, c_0 is its initial value, and $\Delta\ell_{e,c}$ is the prestretch. As a result, the relationship between the axial force $P_{\text{cs}}(\ell_e)$ and the displacement u is expressed as:

$$P_{\text{cs}} = \begin{cases} P_{\text{cs}}(b(u,\varphi) - b_0 + \Delta\ell_{e,b}), & \text{for mountain creases,} \\ P_{\text{cs}}(c(u,\varphi) - c_0 + \Delta\ell_{e,c}), & \text{for valley creases.} \end{cases} \tag{54}$$

Thus, the elastic energy of the nonlinear spring is expressed as (cf. Eq. 26 for the linear case):

$$\begin{aligned} \boxed{U_{\text{spr}}(u,\varphi) = n_{e,b}\text{sgn}(b(u,\varphi)-b_0+\Delta\ell_{e,b})\int_0^{b(u,\varphi)-b_0+\Delta\ell_{e,b}} P_{\text{cs}}(\ell_{e,0}+x_1)dx_1} \\ \boxed{+ n_{e,c}\text{sgn}(c(u,\varphi)-c_0+\Delta\ell_{e,c})\int_0^{c(u,\varphi)-c_0+\Delta\ell_{e,c}} P_{\text{cs}}(\ell_{e,0}+x_2)dx_2.} \end{aligned} \tag{55}$$

The total elastic energy of the nonlinear crease stretch model, $U_{\text{fru}}(u,\varphi)$, is given by the combination of the elastic energy stored in the nonlinear springs and the energy of the standard Kresling cell:

$$\begin{aligned} U_{\text{fru}}(u,\varphi) &= n_{e,b}\text{sgn}(b(u,\varphi)-b_0+\Delta\ell_{e,b})\int_0^{b(u,\varphi)-b_0+\Delta\ell_{e,b}} P_{\text{cs}}(\ell_{e,0}+x)dx \\ &+ n_{e,c}\text{sgn}(c(u,\varphi)-c_0+\Delta\ell_{e,c})\int_0^{c(u,\varphi)-c_0+\Delta\ell_{e,c}} P_{\text{cs}}(\ell_{e,0}+x)dx + \frac{1}{2}n_b k_{s,b}(b(u,\varphi)-b_0)^2 \\ &+ \frac{1}{2}n_c k_{s,c}(c(u,\varphi)-c_0)^2 + \frac{1}{2}n_a k_{r,a}(\delta_a(u,\varphi)-\delta_{a0})^2 + \frac{1}{2}n_b k_{r,b}(\delta_b(u,\varphi)-\delta_{b0})^2 + \frac{1}{2}n_c k_{r,c}(\delta_c(u,\varphi)-\delta_{c0})^2, \end{aligned} \tag{56}$$

We derive the axial force and torque by substituting Eq. 56 into the expressions $\partial U_{\text{fru}}(u,\varphi)/\partial u$ and $\partial U_{\text{fru}}(u,\varphi)/\partial \varphi$. The resulting expression for the axial force is given as:

$$
\begin{aligned}
F(u,\varphi) &= \frac{\partial U_{\text{fru}}(u,\varphi)}{\partial u} \\
&= n_{e,b}\text{sgn}(b(u,\varphi)-b_0+\Delta\ell_{e,b})P_{\text{cs}}(\ell_{e,0}+b(u,\varphi)-b_0+\Delta\ell_{e,b})\frac{\partial b(u,\varphi)}{\partial u} \\
&+ n_{e,c}\text{sgn}(c(u,\varphi)-c_0+\Delta\ell_{e,c})P_{\text{cs}}(\ell_{e,0}+c(u,\varphi)-c_0+\Delta\ell_{e,c})\frac{\partial c(u,\varphi)}{\partial u} \\
&+ n_b k_{s,b}(b(u,\varphi)-b_0)\frac{\partial b(u,\varphi)}{\partial u} + n_c k_{s,c}(c(u,\varphi)-c_0)\frac{\partial c(u,\varphi)}{\partial u} + n_a k_{r,a}(\delta_a(u,\varphi)-\delta_{a0})\frac{\partial \delta_a(u,\varphi)}{\partial u} \\
&+ n_b k_{r,b}(\delta_b(u,\varphi)-\delta_{b0})\frac{\partial \delta_b(u,\varphi)}{\partial u} + n_c k_{r,c}(\delta_c(u,\varphi)-\delta_{c0})\frac{\partial \delta_c(u,\varphi)}{\partial u},
\end{aligned}
\tag{57}
$$

and for the torque is given as:

$$
\begin{aligned}
T(u,\varphi) &= \frac{\partial U_{\text{fru}}(u,\varphi)}{\partial \varphi} \\
&= n_{e,b}\text{sgn}(b(u,\varphi)-b_0+\Delta\ell_{e,b})P_{\text{cs}}(\ell_{e,0}+b(u,\varphi)-b_0+\Delta\ell_{e,b})\frac{\partial b(u,\varphi)}{\partial \varphi} \\
&+ n_{e,c}\text{sgn}(c(u,\varphi)-c_0+\Delta\ell_{e,c})P_{\text{cs}}(\ell_{e,0}+c(u,\varphi)-c_0+\Delta\ell_{e,c})\frac{\partial c(u,\varphi)}{\partial \varphi} \\
&+ n_b k_{s,b}(b(u,\varphi)-b_0)\frac{\partial b(u,\varphi)}{\partial \varphi} + n_c k_{s,c}(c(u,\varphi)-c_0)\frac{\partial c(u,\varphi)}{\partial \varphi} + n_a k_{r,a}(\delta_a(u,\varphi)-\delta_{a0})\frac{\partial \delta_a(u,\varphi)}{\partial \varphi} \\
&+ n_b k_{r,b}(\delta_b(u,\varphi)-\delta_{b0})\frac{\partial \delta_b(u,\varphi)}{\partial \varphi} + n_c k_{r,c}(\delta_c(u,\varphi)-\delta_{c0})\frac{\partial \delta_c(u,\varphi)}{\partial \varphi}.
\end{aligned}
\tag{58}
$$

Crease rotation model (nonlinear, local). In this frustration model, the spring torque–rotation relationship is defined as $T_{\text{cr}} = T_{\text{cr}}(\eta_e)$, where T_{cr} is the torque and η_e is the current rotation of the spring. The spring rotation is given by $\eta_e = \eta_{e,0} + x$ with $\eta_{e,0}$ being the rest angle and x the angular deformation. Since the torsional springs are inserted along the creases, the spring deformation x is given by $x = (\delta_i(u,\varphi) - \delta_{i0} + \Delta\eta_{e,i})$ where $\delta_i(u,\varphi)$ is the current dihedral angle, δ_{i0} is the rest angle, $\Delta\eta_{e,i}$ is the prestress, and $i = a, b,$ or c corresponds to edge, mountain, and valley creases, respectively. Accordingly, the external load applied through the torsional springs is expressed as:

$$
T_{\text{cr}} = T_{\text{cr}}(\delta_i(u,\varphi) - \delta_{i0} + \Delta\eta_{e,i}), \quad i = a,\ b,\ \text{and } c. \tag{59}
$$

Thus, the elastic energy of the nonlinear spring is expressed as (cf. Eq. 35 for the linear case):

$$
\boxed{U_{\text{spr}}(u,\varphi) = \sum_{i=a,\ b,\ c} n_{e,i}\text{sgn}(\delta_i(u,\varphi)-\delta_{i0}+\Delta\eta_{e,i})\int_0^{\delta_i(u,\varphi)-\delta_{i0}+\Delta\eta_{e,i}} T_{\text{cr}}(\eta_{e,0}+x)dx.} \tag{60}
$$

The total elastic energy of the nonlinear crease rotation model is given by:

$$
\begin{aligned}
U_{\text{fru}}(u,\varphi) &= \sum_{i=a,\ b,\ c} n_{e,i}\int_0^{\delta_i(u,\varphi)-\delta_{i0}+\Delta\eta_{e,i}} T_{\text{cr}}(\eta_{e,0}+x)dx + \frac{1}{2}n_b k_{s,b}(b(u,\varphi)-b_0)^2 + \frac{1}{2}n_c k_{s,c}(c(u,\varphi)-c_0)^2 \\
&+ \frac{1}{2}n_a k_{r,a}(\delta_a(u,\varphi)-\delta_{a0})^2 + \frac{1}{2}n_b k_{r,b}(\delta_b(u,\varphi)-\delta_{b0})^2 + \frac{1}{2}n_c k_{r,c}(\delta_c(u,\varphi)-\delta_{c0})^2,
\end{aligned}
\tag{61}
$$

We derive the axial force and torque by substituting Eq. 61 into the expressions $\partial U_{\text{fru}}(u,\varphi)/\partial u$ and $\partial U_{\text{fru}}(u,\varphi)/\partial \varphi$. The resulting expression for the axial force is given as:

$$
\begin{aligned}
F(u,\varphi) &= \frac{\partial U_{\text{fru}}(u,\varphi)}{\partial u} \\
&= \sum_{i=a,\ b,\ c} n_{e,i}T_{\text{cr}}(\eta_{e,0}+\delta_i(u,\varphi)-\delta_{i0}+\Delta\eta_{e,i})\frac{\partial \delta_i(u,\varphi)}{\partial u} + n_b k_{s,b}(b(u,\varphi)-b_0)\frac{\partial b(u,\varphi)}{\partial u} \\
&+ n_c k_{s,c}(c(u,\varphi)-c_0)\frac{\partial c(u,\varphi)}{\partial u} + n_a k_{r,a}(\delta_a(u,\varphi)-\delta_{a0})\frac{\partial \delta_a(u,\varphi)}{\partial u} \\
&+ n_b k_{r,b}(\delta_b(u,\varphi)-\delta_{b0})\frac{\partial \delta_b(u,\varphi)}{\partial u} + n_c k_{r,c}(\delta_c(u,\varphi)-\delta_{c0})\frac{\partial \delta_c(u,\varphi)}{\partial u},
\end{aligned}
\tag{62}
$$

and for the torque is given as:

$$
\begin{aligned}
T(u,\varphi) &= \frac{\partial U_{\mathrm{fru}}(u,\varphi)}{\partial \varphi} \\
&= \sum_{i=a,\ b,\ c} n_{e,i} T_{\mathrm{cr}}(\eta_{e,0} + \delta_i(u,\varphi) - \delta_{i0} + \Delta\eta_{e,i}) \frac{\partial \delta_i(u,\varphi)}{\partial \varphi} + n_b k_{s,b}(b(u,\varphi) - b_0) \frac{\partial b(u,\varphi)}{\partial \varphi} \\
&+ n_c k_{s,c}(c(u,\varphi) - c_0) \frac{\partial c(u,\varphi)}{\partial \varphi} + n_a k_{r,a}(\delta_a(u,\varphi) - \delta_{a0}) \frac{\partial \delta_a(u,\varphi)}{\partial \varphi} \\
&+ n_b k_{r,b}(\delta_b(u,\varphi) - \delta_{b0}) \frac{\partial \delta_b(u,\varphi)}{\partial \varphi} + n_c k_{r,c}(\delta_c(u,\varphi) - \delta_{c0}) \frac{\partial \delta_c(u,\varphi)}{\partial \varphi}.
\end{aligned}
\tag{63}
$$

3. Experimental Data and Error Analysis

For the experimental results in Fig. 3, the black solid curve represents the mean response obtained from five independent tests conducted on standard Kresling samples. The colored solid curves (red, blue, and orange) represent the mean responses from three tests, each performed on a different frustrated Kresling sample with distinct prestress configurations. The mean values of displacement u_i, rotation φ_i, force F_i, torque T_i, and energy U_i at the i-th loading step are computed as follows (3):

$$
u_i = \frac{\sum_{j=1}^{n_c} u_i^j}{n_c},\ \varphi_i = \frac{\sum_{j=1}^{n_c} \varphi_i^j}{n_c},\ F_i = \frac{\sum_{j=1}^{n_c} F_i^j}{n_c},\ T_i = \frac{\sum_{j=1}^{n_c} T_i^j}{n_c},\ U_i = \frac{\sum_{j=1}^{n_c} U_i^j}{n_c},
\tag{64}
$$

where u_i^j, φ_i^j, F_i^j, T_i^j, and U_i^j are the displacement, rotation, force, torque, and energy values recorded from the j-th sample at the i-th loading step, and n_c is the number of samples used for each configuration ($n_c = 5$ for the standard Kresling cell and $n_c = 3$ for the frustrated Kresling cell). The shaded regions around each curve represent the standard deviation of force $\sigma_{F,i}$, torque $\sigma_{T,i}$, and energy $\sigma_{U,i}$, across the n_c Kresling samples. These standard deviations are calculated as follows:

$$
\sigma_{F,i} = \sqrt{\frac{\sum_{j=1}^{n_c} |F_i^j - F_i|^2}{n_c - 1}},\ \sigma_{T,i} = \sqrt{\frac{\sum_{j=1}^{n_c} |T_i^j - T_i|^2}{n_c - 1}},\ \sigma_{U,i} = \sqrt{\frac{\sum_{j=1}^{n_c} |U_i^j - U_i|^2}{n_c - 1}}.
\tag{65}
$$

Additionally, since the initial displacement (or rotation) is not prescribed but rather estimated from the experimental measurements, the initial points of the curves include error bars in both the vertical and horizontal directions, as shown in Figs. 3B, D, and F. Specifically, the horizontal error bars represent the standard deviation of the displacement $\sigma_{u,i}$ (or of the rotation $\sigma_{\varphi,i}$) at the initial loading step, i.e., $i = 1$. These standard deviations are calculated as follows:

$$
\sigma_{u,1} = \sqrt{\frac{\sum_{j=1}^{n_c} |u_1^j - u_1|^2}{n_c - 1}},\ \sigma_{\varphi,1} = \sqrt{\frac{\sum_{j=1}^{n_c} |\varphi_1^j - \varphi_1|^2}{n_c - 1}}.
\tag{66}
$$

4. Discussion on Differences between Theoretical Analyses and Experimental Results

The differences between theoretical analyses and experimental results are present in all frustrated models in Fig. 3, which stem from three primary challenges. The first major challenge is panel buckling and bending during folding. As the Kresling structure deforms, panels can buckle in ways that are difficult to predict theoretically. Even advanced computational methods like finite element analysis struggle to capture this behavior accurately because buckling often occurs suddenly and can follow multiple possible deformation paths. The second challenge involves contact interactions between panels during folding. When different parts of the structure come into contact, they create complex friction forces and localized stress distributions. These interactions are highly sensitive to small variations in alignment, material properties, and surface conditions, making them exceptionally difficult to model with precision. The third and perhaps most significant challenge comes from manufacturing imperfections. While theoretical models assume perfect adhesion between rigid surfaces, real-world samples inevitably contain small gaps, uneven bonding, or minor misalignments. These imperfections can trigger unexpected buckling modes that diverge from theoretical predictions. Moreover, we observe from Fig. 3 that experimental results for global frustration mechanisms show better agreement with theory compared to crease (local) frustration cases. This difference occurs because crease (local) frustration is more sensitive to the imperfections and modeling challenges described above. Nevertheless, our results provide valuable insights into the mechanics of crease-frustrated cells, particularly in understanding how frustration modifies the energy landscape of the system.

5. Experiment on Crease (Local) Stretch Model (Positive Mode)

We develop a modular fabrication protocol to realize the local stretch model with positive prestress, incorporating spring elements, wire connectors, 3D-printed frames, and handles (Fig. S4A). The handle is used to control the level of prestress in the spring. The spring extension, $\Delta\ell$, depends on the handle radius r_{handle} and the number of interval turns n, and is defined as: $\Delta\ell = n(2\pi r_{\mathrm{handle}})/12$. The prestressed spring deforms the standard Kresling cell into a new equilibrium configuration, which

has a non-zero base energy due to both the deformed origami cell and the spring. By tuning the prestress, the base energy of the initial stable states can be controlled, as shown in Fig. S4B (top-left). In compression experiments using a free-rotating fixture, we tested two different spring extensions and compared them with the standard Kresling cell. The results show that the shape of the energy landscape depends on the spring extension: greater extension leads to a higher energy barrier for the frustrated cell. This observation is consistent with the theoretical predictions shown in Fig. S4B (bottom-left).

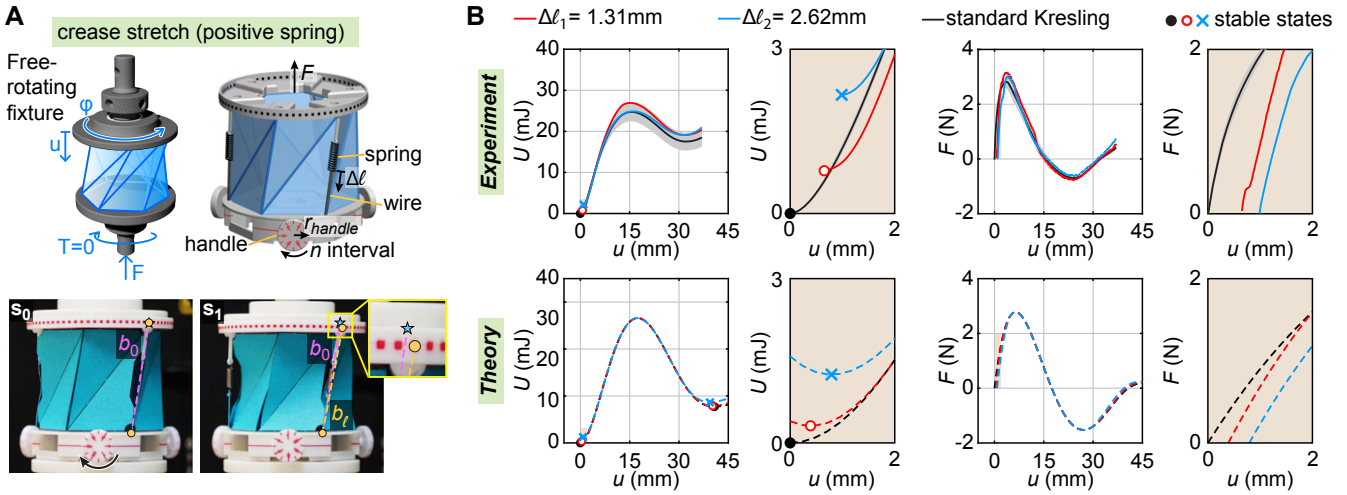

Fig. S4. Experiment of crease stretch frustrated model with positive prestress. (A) Top-left: illustration of axial loading with a free-rotating fixture. Top-right: schematic of the design enabling prestress along some mountain creases. Bottom-left: photo of an undeformed origami cell. Bottom-right: photo of a prestressed unit in its initial stable state. (B) Experimental results and theoretical predictions. Top: experimental results comparing the behavior of the frustrated models with the standard origami cell. The black curve is the mean value of five experiments, and the grey-shaded area represents the standard deviation. The red and blue colors represent different prestress levels. Bottom: corresponding theoretical predictions. Left: axial displacement u versus stored elastic energy U. Right: displacement versus applied forces F. The insets highlight the early stages of the tests.

6. Non-parallel Plates in Standard Kresling Assemblies

In Movie S5, we observe that the 3D-printed plates between the cells of a standard Kresling assembly become non-parallel during the axially constrained twist experiment. To investigate this behavior, we compare the results from Movie S5 with those from an alternative folding path under the same loading conditions (Fig. 4), as well as with results obtained from an assembly constructed using newly fabricated cells. Fig. S5A shows the folding path from [0 1 0] to [1 0 0] for both the old and new specimens. In the old specimen, two discs become visibly non-parallel, whereas in the new specimen, only one disc exhibits this behavior, resulting in noticeable differences in the corresponding torque curves. This comparison suggests that fabrication errors are a contributing factor to the non-parallel behavior.

Additionally, we compare the results in Fig. S5A with those in Fig. S5B. In the latter case, the red cells at the bottom remain deployed throughout the experiment, providing stable support for the yellow and blue cells above. Consequently, non-parallel deformation is less pronounced. In contrast, the red cell in Fig. S5A remains folded during testing. Because the folded configuration is less stiff than the deployed one, it cannot adequately support the upper cells, leading to more significant non-parallel deformation.

7. Fixture Selection in Experiments of Assemblies

Figure 4 shows that the folding and deploying processes of the Kresling assembly are activated by four boundary conditions, including rotationally constrained fixture, free-rotating fixture, axially constrained fixture, and free-translating fixture. The selection of the fixture is based on three conditions: the number of cells in the assembly, the geometric chirality of the Kresling cell, and the intrinsic coupling between axial displacement and rotation. Here, we propose three rules of choosing a fixture with illustrative examples in Fig. 4. Rule number one is that we use either free-rotating (folding path ⑥ and ⑧) or free-translating (folding path ② and ④) fixtures to sequentially fold single cells in an array because these fixtures can decouple the axial displacement and twist of the single cell. Rule number two is that we use either rotationally constrained (folding path ① and ⑦) or axially constrained fixtures (folding path ③ and ⑤) to simultaneously fold two cells with opposite chirality in the array. Rule number three is that we use the free-translating fixture to fold a cell in a dipole (two cells with opposite chirality but same energy barrier) in the array (folding path ② and ④). In summary, the complex, coupled kinematics of the Kresling structure makes the folding process highly sensitive to the end conditions. As such, precise control over the folding sequence (enabled by the correct fixture setup) is essential when using Kresling cells in applications that rely on predictable and programmable mechanical responses.

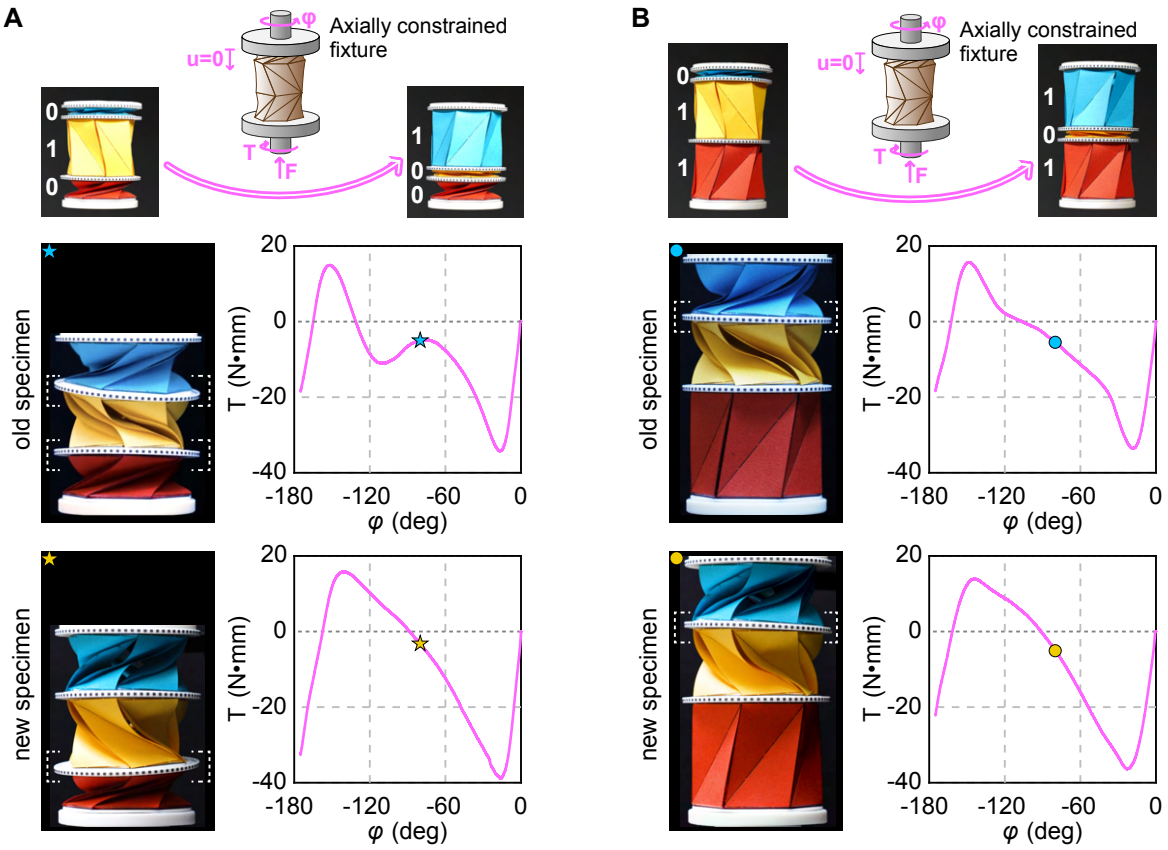

Fig. S5. Illustration of non-parallel plates in standard Kresling assemblies. (A) Folding path from [0 1 0] to [1 0 0] performed using both old and newly fabricated specimens. Snapshots of the old specimen correspond to 2:01–2:10 minutes in Supplementary Video 5. (B) Folding path from [0 1 1] to [1 0 1] achieved with the old and new specimens.

8. Energy Landscape of Kresling Arrays

Figures S6 and S7 show the energy landscapes of the non-frustrated and frustrated Kresling arrays, respectively. The energy landscape of the non-frustrated arrays is computed using the following formulation:

$$U_{\text{exp, F}} = \sum_{i=1}^{n} (u_{\text{exp},i+1} - u_{\text{exp},i-1}) F_{\text{exp},i}/2, \quad U_{\text{exp, T}} = \sum_{i=1}^{n} (\varphi_{\text{exp},i+1} - \varphi_{\text{exp},i-1}) T_{\text{exp},i}/2, \tag{67}$$

where $F_{\text{exp},i}$, $u_{\text{exp},i}$, $T_{\text{exp},i}$, and $\varphi_{\text{exp},i}$ represent the experimental force, axial displacement, torque, and twist angle at the i-th loading step (with n loading steps in total), respectively. The energy of the frustrated arrays is given by:

$$U_{\text{exp, F}} = \sum_{j=1}^{3} U_{\text{fru},j} + \sum_{i=1}^{n} (u_{\text{exp},i+1} - u_{\text{exp},i-1}) F_{\text{exp},i}/2, \quad U_{\text{exp, T}} = \sum_{j=1}^{3} U_{\text{fru},j} + \sum_{i=1}^{n} (\varphi_{\text{exp},i+1} - \varphi_{\text{exp},i-1}) T_{\text{exp},i}/2, \tag{68}$$

where $U_{\text{fru},1}$, $U_{\text{fru},2}$, and $U_{\text{fru},3}$ denote the base energy at the first stable state for the blue, yellow, and red frustrated cells, respectively. The base energies of the cells in the frustrated Kresling array are defined as: $U_{\text{fru},1} = U_{\text{fru},2} = 5.46$ mJ and $U_{\text{fru},3} = 15.61$ mJ.

9. Reprogramming Frustrated Kresling Assemblies

To demonstrate the reprogrammability enabled by the frustrated Kresling assemblies, we consider an array composed of three frustrated cells, where the prestress level of the bottom cell is controlled via a torsional (global) spring (Fig. S8A). The markers on the handle indicate the applied prestress level. We conduct three experiments with varying prestress conditions in the bottom cell (Fig. S8B). Two distinct folding paths, labeled path ① and path ②, are observed, as shown in Fig. S8B (top and middle). Interestingly, although path ② and path ③ follow identical folding sequences (Fig. S8B - middle and bottom), their corresponding energy landscapes and torque–twist angle profiles differ significantly (Fig. S8C). These results confirm that both the folding path and energy barrier of multi-cell arrays can be actively reprogrammed by adjusting the prestress configuration.

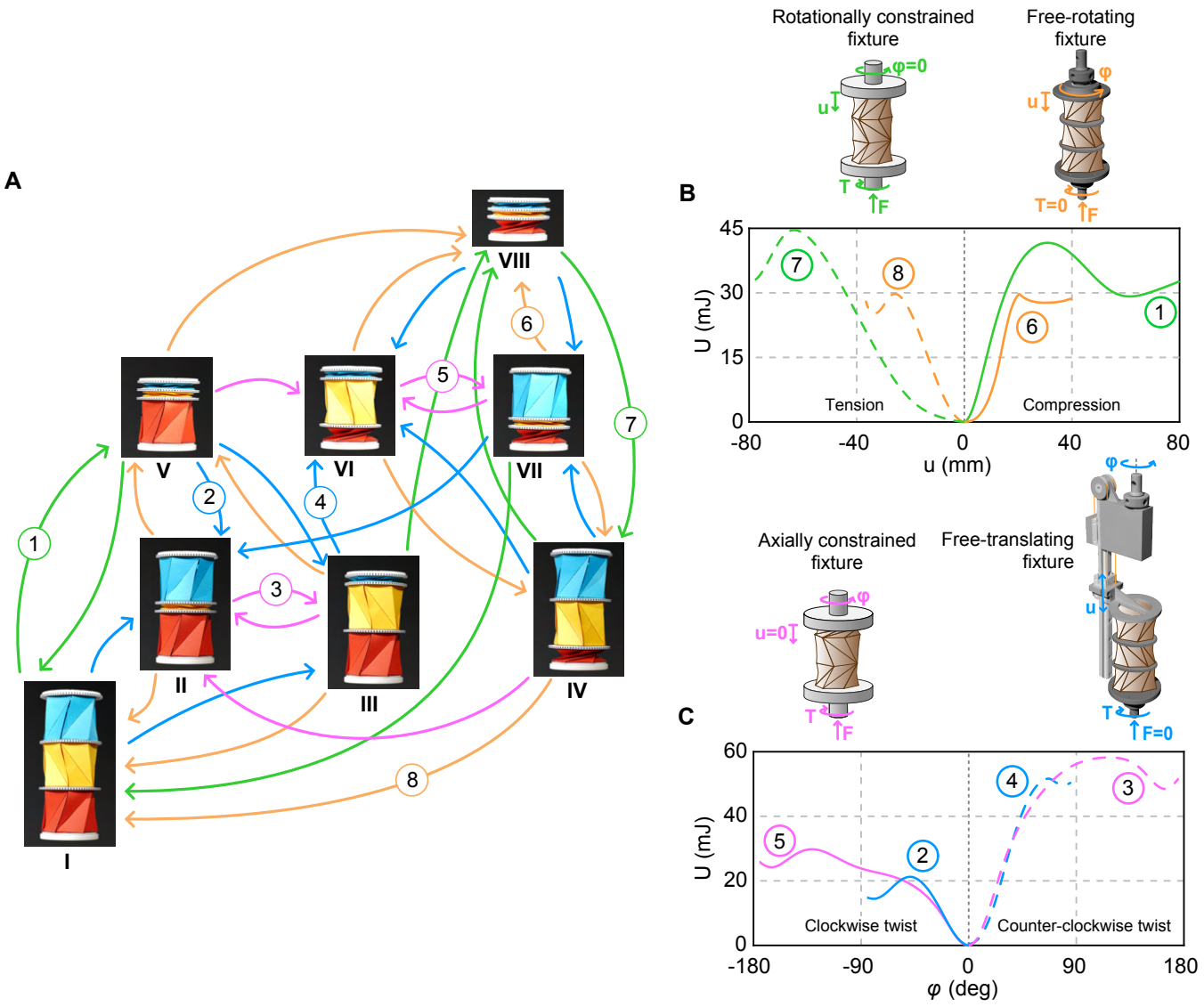

Fig. S6. Energy curves of the three-cell array without frustration. (A) Feasible folding paths. (B) Energy curves obtained from experimental results associated with the rotationally constrained fixture and the free-rotating fixture. The circled numbers in the plot correspond to those in panel (A). (C) Energy curves obtained from experimental results associated with the axially constrained fixture and the free-translating fixture. The circled numbers in the plot correspond to those in panel (A).

10. Frustrated and Non-frustrated Curved-crease Origami

Figure S9 shows the snapshots captured from the compression test of frustrated and non-frustrated curved-crease origami tubes, respectively. The two origami tubes have similar configurations at displacement $u = 0$mm and 0.48mm. However, the deformations of two origmai tubes at $u = 2.5$mm are quite different, which indicates different behaviors of frustrated and non-frustrated curved-crease origami tubes.

11. Panel Buckling in Programmable Non-commutative States

The experimental data of non-frustrated Kresling array in Fig. 6B (top) shows a jagged portion on the unloading curve under clockwise twist, see state i to state iii in Fig. S10 (left). This phenomenon is caused by the panel buckling and recovery observed in the yellow cell. The buckling deformation is referring to the valley creases popping out of the panels, as shown in the snapshots (Fig. S10, right). At state i, all six panels of the cell are buckled. At state ii, several panels recover while the others are still buckled. Finally, all panels recover at state iii.

12. Materials and Methods

Fabrication of Kresling origami cells. Both the standard and frustrated origami cells were fabricated using a multilayer material composed of Tant origami paper and 0.17 mm-thick adhesive tape (3M 9474LE). The blue and yellow cells consist of two layers

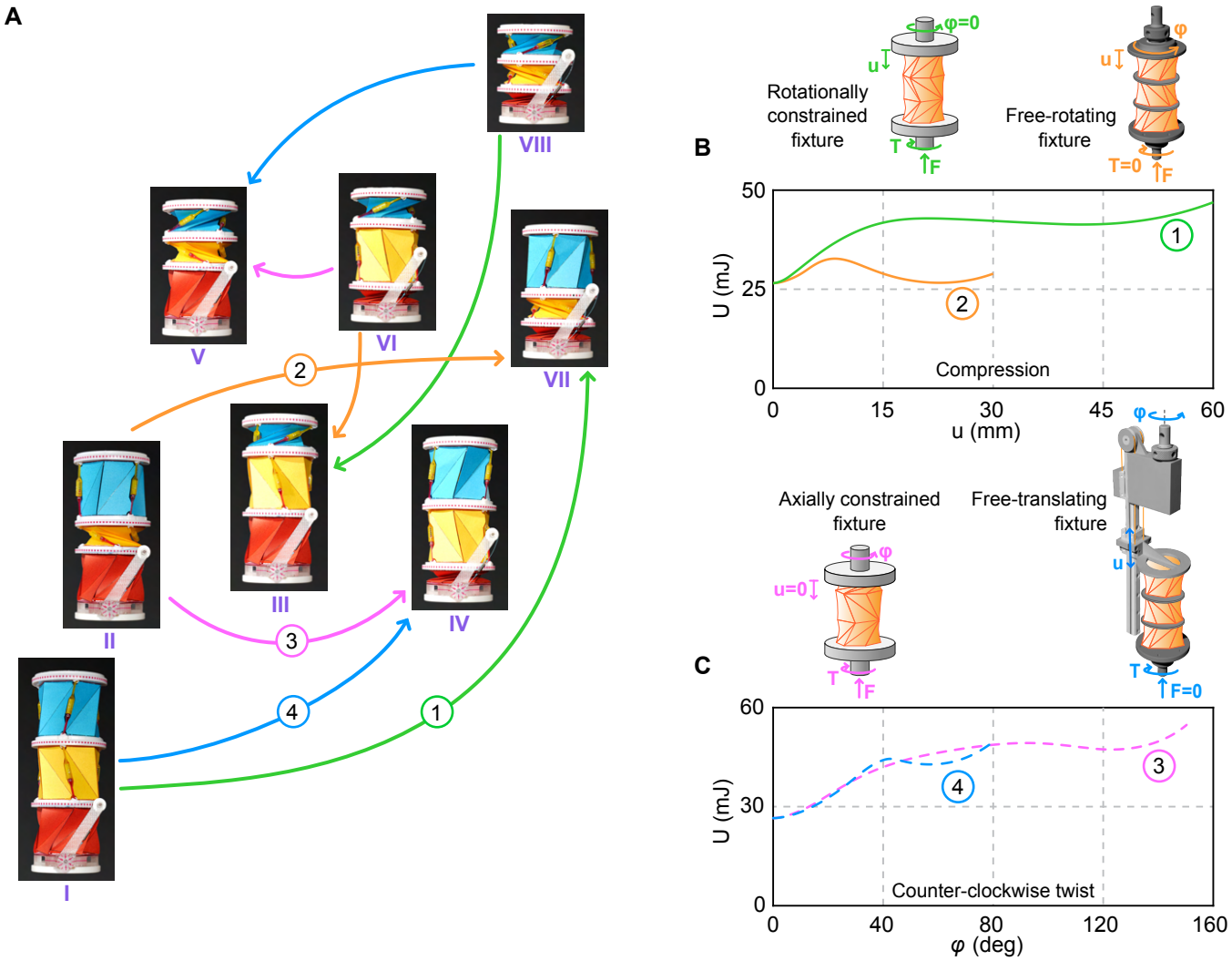

Fig. S7. Energy curves of the three-cell array with frustration. (A) Feasible folding paths. (B) Energy curves obtained from experimental results associated with the rotationally constrained fixture and the free-rotating fixture. The circled numbers in the plot correspond to those in panel (A). (C) Energy curves obtained from experimental results associated with the axially constrained fixture and the free-translating fixture. The circled numbers in the plot correspond to those in panel (A).

of origami paper and one intermediate adhesive layer, as shown in Fig. S11A. The red cell uses a stiffer configuration with three layers of origami paper and two layers of adhesive tape (Fig. S11C). All mountain creases were cut to facilitate folding. For the crease (local) stretch design, a trapezoidal hole was introduced into the panel (Fig. S11B) to prevent interference between the prestressed spring element and the origami structure.

Fabrication of prestressed elements. The 3D-printed prestressed components were fabricated using a Stratasys J55 Prime PolyJet printer. For the global stretch model, the frames and handle were printed using VeroWhite material, while the markers were printed using VeroMagenta. In the global rotation model, the top frame and markers used the same materials as in the global stretch model, but the bottom frame and handle were printed with VeroUltraClear. For the crease (local) stretch model, the frames and markers were printed with the same materials used in the global stretch model. Additionally, the casing assembled on the top and bottom frames was printed using VeroYellow and VeroMagenta, respectively. The pulley used in the global rotation model is a ball bearing pulley (MiSUMi, SZV3-12). The extension spring used in the global stretch model has a stiffness of 0.3 N/mm (McMaster-Carr, 9065K566). The global rotation model uses an extension spring with a stiffness of 0.21 N/mm (McMaster-Carr, 5108N036). In the crease (local) stretch model, the spring used in the negative mode is a compression spring with a stiffness of 0.46 N/mm (McMaster-Carr, 9657K641), while the spring used in the positive mode is an extension spring with a stiffness of 0.22 N/mm (McMaster-Carr, 1942N36)*. The springs in both global models and the local stretch model (positive mode) are connected to the 3D-printed components using 0.3 mm diameter fishing wire.

All prestressing systems mentioned in both main text and SI Appendix can be manufactured by standard 3D printers, which enhances the practicality of our concept. As an example, Fig. S12 shows the design of a 3D-printed frustrated Kresling cell

*More details can be found on https://www.mcmaster.com/products/springs/springs-2 /

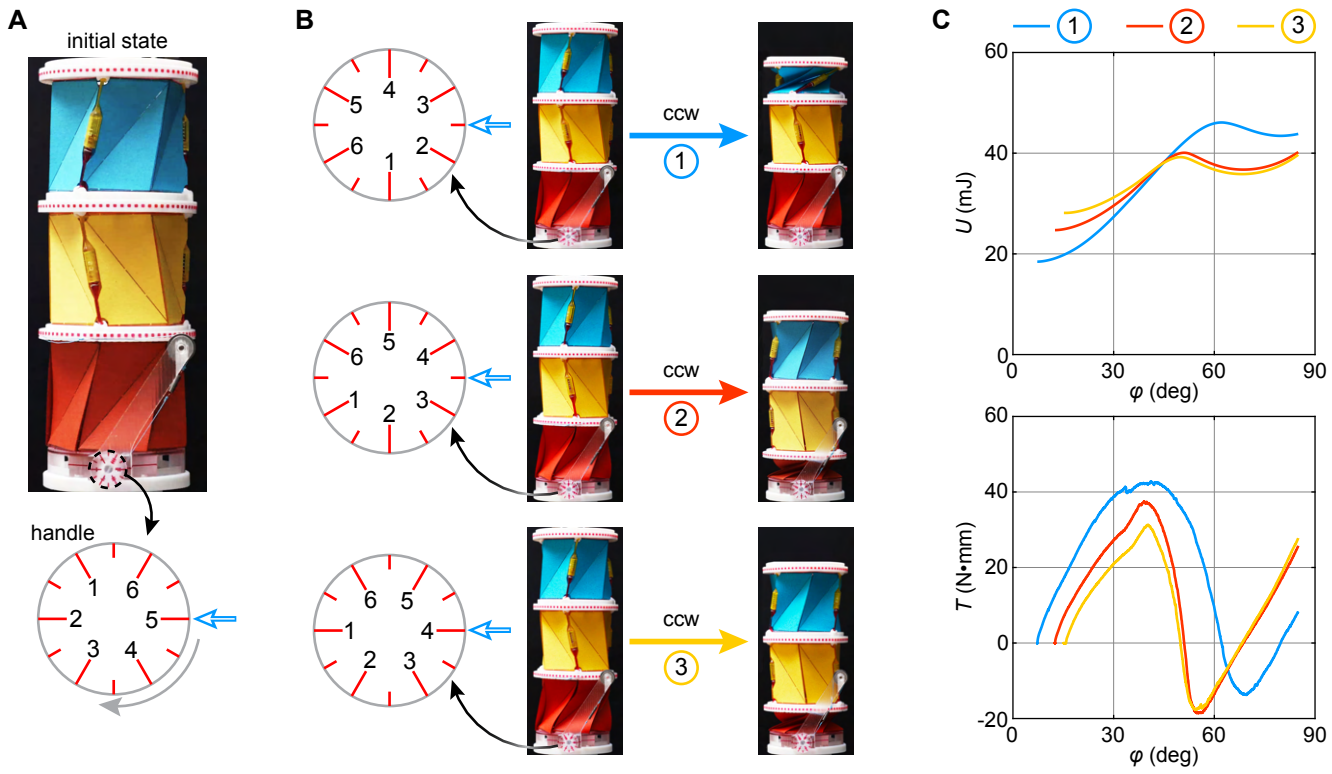

Fig. S8. Reprogrammability of the frustrated 3-cell array. (A) Initial state of the array. (B) Reprogrammability of the folding path. (C) Reprogrammability of the energy landscape.

based on truss model, revealing that our approach can be practical for broader applications involving 3D printing.

Experimental setups. The free-rotating and free-translating experimental setups are illustrated in Fig. S13. Both configurations consist of two fixtures that connect the top and bottom surfaces of the origami cell to the Instron loading frame (Model 68SC-5 Single Column Testing System). The fixtures are attached to the origami cell using multiple miniaturized magnets. In both setups, the bottom fixture is identical and designed to restrain both rotational and axial motion, effectively eliminating any unintended rigid body displacement during testing. Axial load and torque are measured using a biaxial force/torque sensor (±445 N, ±5.65 Nm).

In the free-rotating setup (Fig. S13A), the top fixture allows unrestricted rotation of the origami cell. This is enabled by incorporating a ball bearing (SKF 608, 8×22×7 mm) into the top plate, which permits the natural twisting of the frustrated Kresling structure during compression and tension. These tests are performed at a displacement rate of 0.25 mm/s.

In the free-translating setup (Fig. S13B), the top fixture enables axial movement while allowing the structure to rotate freely. This is achieved using a linear rail system with two sliders that support a translating top plate, minimizing friction and preventing rigid coupling. A pulley system is added to counterbalance the weight of the translating plate, preventing it from imposing unwanted axial forces on the origami cell that could bias the measurement of bistability. Torsional experiments in this setup are conducted at a rotation rate of 0.5 deg/s.

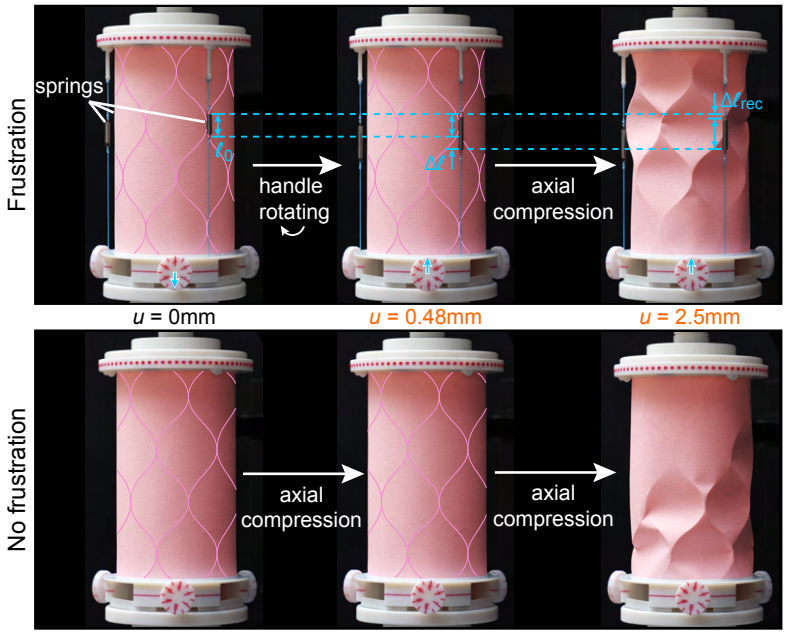

Fig. S9. Snapshots of frustrated (top) and non-frustrated (bottom) curved-crease origami tubes at displacement $u = 0\text{mm}$, 0.48mm, and 2.5mm.

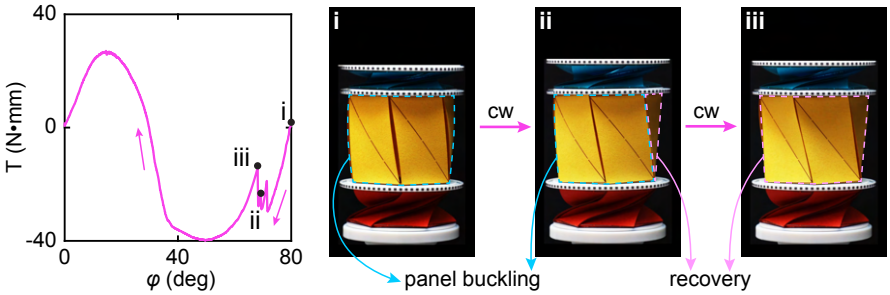

Fig. S10. Illustration of the jagged portion existing in the non-commutative result of non-frustrated Kresling array.

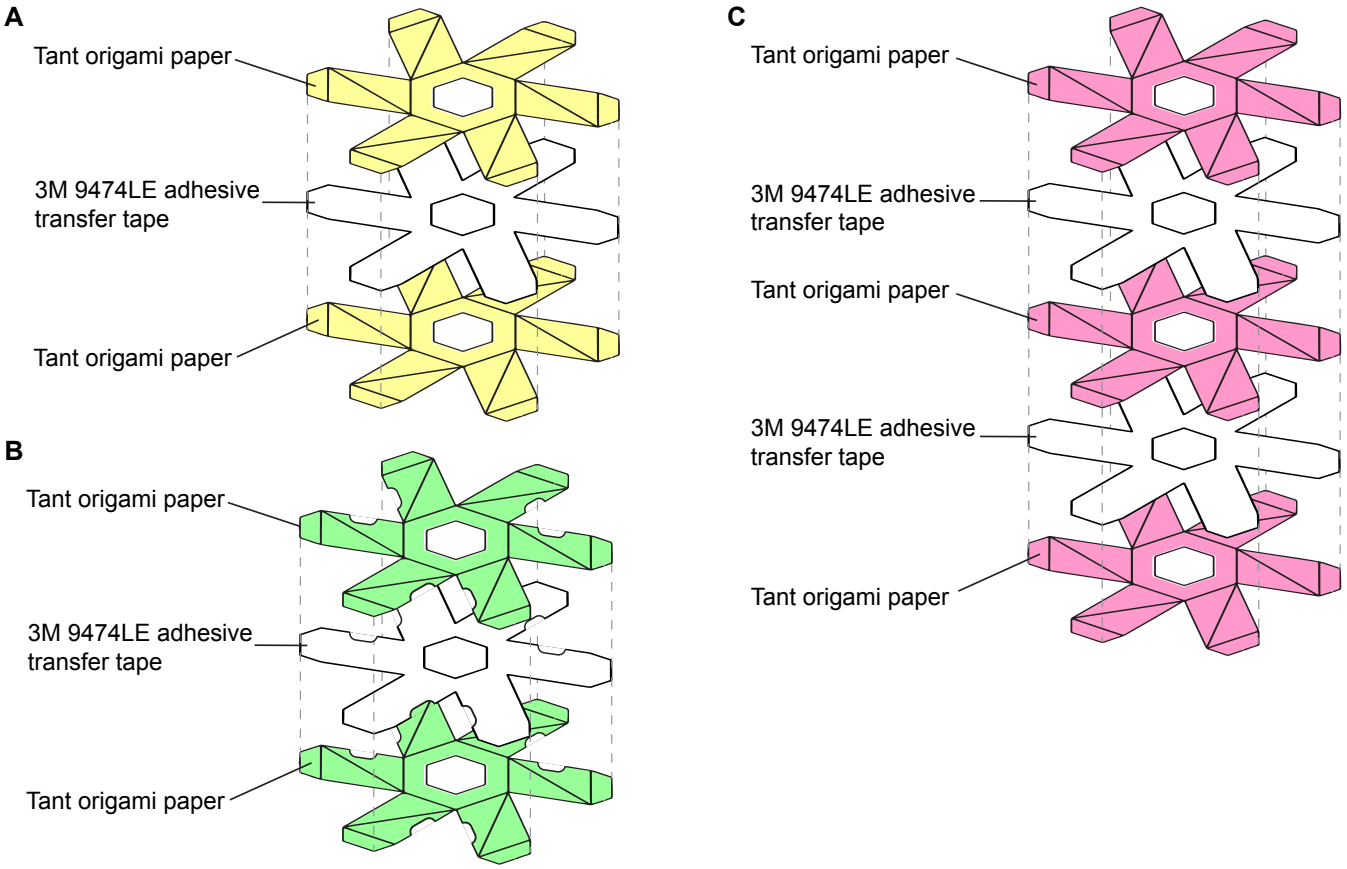

Fig. S11. Fabrication details of standard and frustrated Kresling origami cells. (A) Blue and yellow cells used in experiments for the standard and globally frustrated models. (B) Blue and yellow cells used in experiments for the crease-level (local) frustration model.(C) Red cell used in both standard and frustrated Kresling assemblies.

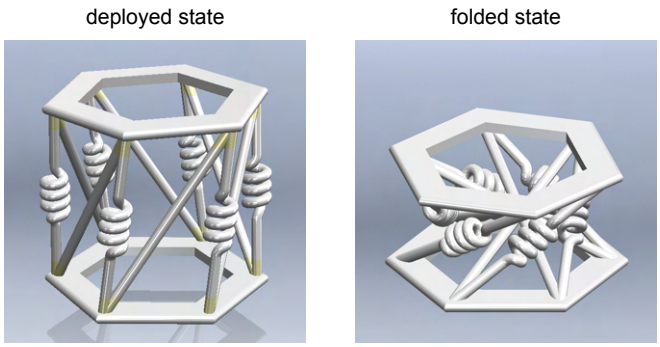

Fig. S12. 3D-printed frustrated Kresling cell.

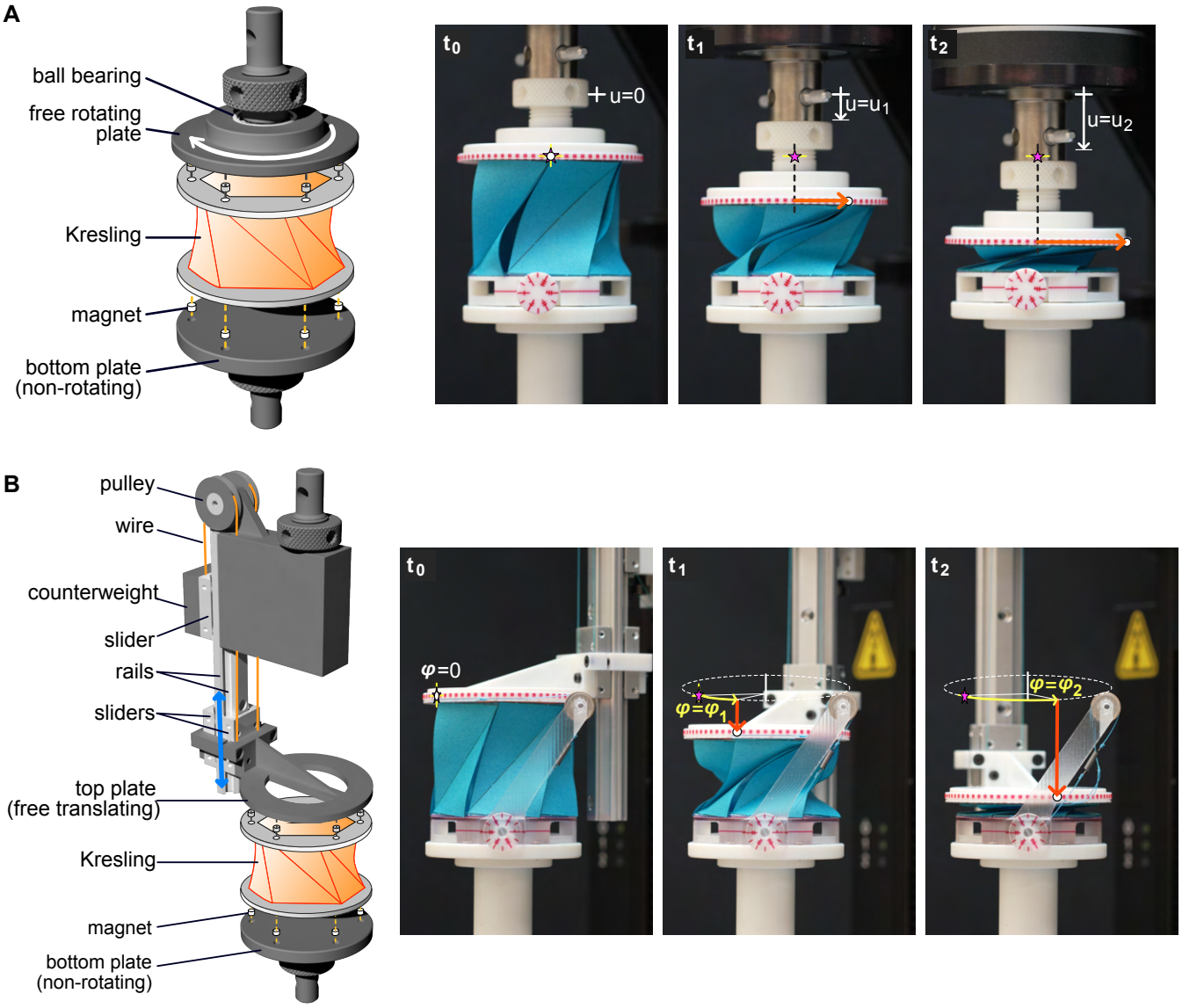

Fig. S13. Details of the free-rotating and free-translating fixtures designed for conducting compression and torsional experiments, respectively. (A) Left: schematics of the free-rotating fixture (reproduced from Ref. (1)). Right: snapshots extracted from the record of the experiment at different times illustrating the working principles of the setup. Compression on the Kresling array is achieved by imposing the axial displacement u, indicated by white arrows, using a loading frame machine. The fixture enables free rotation, facilitating the natural twisting of the Kresling, as indicated by the red arrows. (B) Left: schematics of the free-translating fixture (reproduced from Ref. (1)). Right: snapshots extracted from the record of the experiment at different times illustrating the working principles of the setup. Twisting in the Kresling array is accomplished by applying a rotation φ, as indicated by yellow arrows, using a loading frame machine. The fixture is connected to a linear slide system that enables unrestricted translation, allowing the Kresling array to undergo axial folding without constraints, as indicated by the red arrows.

Movie S1. Frustration

Movie S2. Frustrated Apparatus - Global Stretch

Movie S3. Frustrated Apparatus - Global Rotation

Movie S4. Frustrated Apparatus - Crease Stretch

Movie S5. Experiments with Non-frustrated Kresling Arrays

Movie S6. Experiments with Frustrated Kresling Arrays

References

1. S Zang, D Misseroni, T Zhao, GH Paulino, Kresling origami mechanics explained: Experiments and theory. *J. Mech. Phys. Solids* **188**, 105630 (2024).
2. M Paredes, E Rodriguez, M Sartor, Analytical behavior law for a constant pitch conical compression spring. *J. Mech. Des.* **128** (2006).
3. J Taylor, *Introduction to Error Analysis, the Study of Uncertainties in Physical Measurements.* (University Science Books), (1997).